ELECTRONIC ENERGY LEVEL ALIGNMENT OF DYE MOLECULES ON TIO$_2$ AND ZNO SURFACES FOR PHOTOVOLTAIC APPLICATIONS

BY JEAN-PATRICK THEISEN

A thesis submitted to the

Graduate School—New Brunswick

Rutgers, The State University of New Jersey

in partial fulfillment of the requirements

for the degree of

Master of Science

Graduate Program in Physics

Written under the direction of

Professor Dr. Robert Bartynski

and approved by

————————————————————

————————————————————

————————————————————

New Brunswick, New Jersey

October, 2008

ABSTRACT OF THE THESIS

ELECTRONIC ENERGY LEVEL ALIGNMENT OF DYE MOLECULES ON TiO$_2$ AND ZnO SURFACES FOR PHOTOVOLTAIC APPLICATIONS

by Jean-Patrick Theisen

Thesis Director: Professor Dr. Robert Bartynski

In dye-sensitized solar cells (DSSC), the attributes of the dye-semiconductor interface are of important interest. In this thesis, electronic and structural aspects of dye/semiconductor systems have been studied experimentally using ultraviolet photoemission spectroscopy (UPS), inverse photo electron spectroscopy (IPS) and scanning tunneling microscopy (STM).

In this work the electronic structure of N3, or more precisely Ru(4,4-dicarboxylate-2,2-bipyridine)$_2$-(NCS)$_2$, molecules absorbed on rutile TiO$_2$(110) single crystal and anatase TiO$_2$ nanoparticles has been studied and has shown that the energy of highest occupied molecular orbital (HOMO) of the N3 dye is located near the middle of the semiconductor band gap and that the lowest unoccupied molecular orbital (LUMO) level overlaps with the Ti 3d orbitals of the TiO$_2$ conduction band. A shift of the UPS/IPS energy spectra indicate the formation of an induced dipole upon N3 adsorption on the TiO$_2$ surface.

The electronic contributions of N3 in combination with ZnO are similar to N3 absorbed on TiO_2. The position of the HOMO is almost identical in regard to the band edge of the valence band, but the LUMO is located a bit higher in energy in regard the conduction band minimum (CBM) as in comparison with $N3/TiO_2$. We studied also the adsorbate isonicotinic acid (INA) with chemical structure: $C_6H_5NO_2$ on the oxides, because it is a good model for the binding ligand of the N3 molecule and which is where the spatial distribution of the N3 LUMO is expected to be delocalized. Indeed, the electronic structure of the LUMO for INA adsorbate is for both semiconductors is very similar to the LUMO of the adsorbate N3 dye.

Another dye, catechol ($C_6H_6O_2$), has been reported that catechol bonds strongly to TiO_2 and that electrons can be excited directly from the catechol HOMO to the conduction band of TiO_2. Our experiments show that the LUMO is indeed mixed significantly with the conduction band of TiO_2.

A monolayer of pivalate ((CH3)3CCOO-) ions was used to protect the sample surface from contamination during the wetting process of the N3 adsorption. The effect of passivation on the quality of the semiconductor/dye interface is studied by UPS and IPS measurements.

Table of Contents

Chapter 1

Introduction

1.1   Introduction and motivation

With constant progress in technology, the power requirement of mankind rises. Currently, fossil fuels are the main source of man-made energy on the earth. Heat is gained by burning these fossil fuels (coal, oil, natural gas), which not only produces atmosphere contamination but also contributes to global warming. This is an environmentally unfriendly energy source that will eventually be depleted. Energy can also be produced by nuclear power plants, which represent the most efficient kind of power production today. This production however generates radioactive by-products, which remain active for a significant period of time. The principle of gaining energy is often the same: heat is produced and converted afterwards into electricity by turbines and water steam.

An alternative to these approaches is to use the sun as an energy source. Solar energy is clean, nearly unlimited and the suns energy can be converted directly into electricity without mechanical parts or noise pollution. The idea to producing electricity from solar energy is not new. For some years there have been stable and efficient solar cells on the market. However, an enormous amount of power is required for the production of these conventional solar cells and it takes years to regain the same amount of energy with these cells. In the last decades, the development of new types of solar cells, above all the small thin film solar cells, is making enormous progress in regard to the conversion efficiency. Unfortunately the manufacturing costs of thin film solar cell components with

high purity are too high, so that they still cannot compete with other energy sources on the present market.

Dye sensitized solar cell (DSSC) is an other promising candidate to collect solar power and intensely investigated at present. This solar cell, which was introduced by Grätzel and co-workers [1] has a nanostructured TiO_2/dye interface as its core. This system, which can be cheaply fabricated, has a big potential to become a low priced and non-toxic source of electric energy. The future development of DSSC needs a deeper understanding of the processes involved. The system is indeed very complex combining organic and inorganic chemistry with surface science. Some of the most important processes take place on a microscopic level, where molecular and electronic characteristics are of great importance. In a DSSC, the dye molecule is responsible for the absorption of light and should thereby be sensitive to a large part of the visible solar spectrum. In this thesis, the main focus is at the identification of the electronic structure of several different dye/semicondutor interfaces. As semiconductors are used rutile $TiO_2(110)$ single crystals, anatase TiO_2 nanoparticles, $ZnO(11\bar{2}0)$ single crystals and ZnO nanopillars; as dye are used N3 (Ru(4,4-dicarboxylate-2,2-bipyridine)$_2$-(NCS)$_2$), INA ($C_6H_5NO_2$) and catechol ($C_6H_6O_2$). We use ultraviolet photoemission spectroscopy (UPS) and inverse photoelectron spectroscopy (IPS) to determine the occupied and unoccupied levels of these systems

1.2 Solar cells

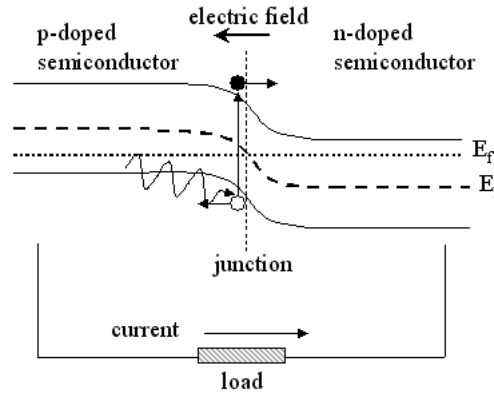### 1.2.1 Traditional Si-Solar cell

Figure 1.1: Scheme of a pn-transition

Due to the world-wide effort to discover alternative energy sources, solar cells, which convert sunlight directly into electrical energy, are subjects of intensive research. In comparison to other energy sources, the production and utilization of solar cells involves less CO_2 emission and no radioactive waste products. The core of a traditional solar cell is a p-n junction (see Fig. 1.1), which generates an electric field across the p-n interface. The n-semiconductor is positively charged and the p-semiconductor is negatively charged in the region of near the interface. When a photon is absorbed in the solar cell, an electron is excited from the valence band to the conduction band and an electron-hole pairs are produced. Electrons and holes are separated by the electric field of the p-n junction. Via the back and front contact, the electrons travel through an outer electric circuit to the p-semiconductor, where they recombine with holes. Efficiency is the main criterion to evaluate solar cells and defined as the ratio of the gained electric power to the absorbed solar power (η). The efficiency of a solar cell is given by the equation 1.1, where P is the electric power, I is the radiation intensity of the incident light and A is the surface area of the solar cell. Silicon solar cells can be made either out of single crystal, polycrystalline or amorphous silicon, having respective efficiencies in panels of 25 %, 18 % and 13 % [3].

The common use of Si solar cells is limited due to the high production costs, particularly with single crystal and polycrystalline solar cells. DSSC have shown an efficiency of 10 %, which, considering their low cost, makes them an attractive alternative to Si solar cells [4].

$$\eta = \frac{P}{IA} \tag{1.1}$$

1.2.2 Dye Sensitized Solar Cells (DSSC)

Dye Sensitized Solar Cells, or so-called Grätzel cells, are based on transition metals or organic dye molecules, which are adsorbed onto a semiconductor. Upon light absorption by the dye, an electron is transferred from the dye HOMO level to the dye LUMO level and injected into the semiconductor. As the semiconductor material, highly porous, nano-crystalline TiO_2 has shown the highest efficiency [2]. In the following, the arrangement of a DCCS is introduced in greater detail.
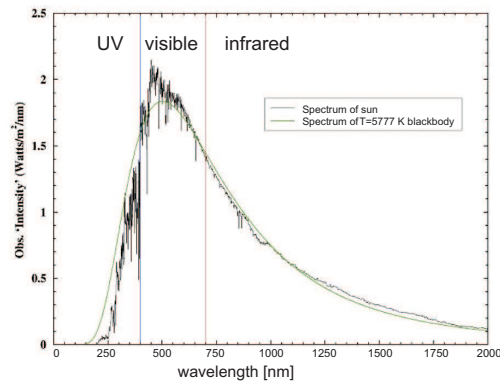
Figure 1.2: Spectrum of the sun and spectrum of a 5777 K blackbody

The body of a DSSC is a multi-layer structure, as shown in Fig. 1.3. The bottom layer consists of glass plate coated with a transparent conducting oxide (TCO), which is typically F doped SnO_2. On this this plate, a porous TiO_2 nanoparticle layer is mounted, known as the electrode. The TiO_2 nanoparticles are coated on all exposed surfaces with a mono-layer of dye molecules and immersed in an electrolytic solution. The top layer of the body of a DSSC is another glass plate, the underside of which is coated with TCO and a bottom layer of Pt. The Pt layer, which is in contact the electrolyte, is known as the counter electrode. The electrode and counter electrode are connected through a load.
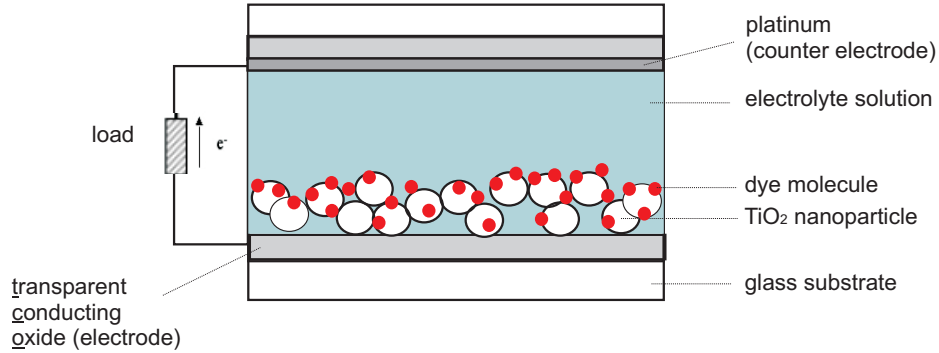
Figure 1.3: Schematic arrangement of a DSSC

The dye molecule is responsible for the absorption of light. Anatase TiO_2 nanoparticles have an optical band gap of 3.2 eV [25] and can only absorb light with wavelengths less than 340nm. Since the optical band gap of of N3 on TiO_2 is about 1.6 eV [49], the N3 dye molecule is able to absorb light in the visible and near infrared spectrum and covers therefore the emission peak of the solar spectrum (550 nm, 2.27 eV), which is shown in Fig 1.2. The HOMO-LUMO gap of the isolated N3 molecule in gas phase is about 0.5 eV (2.48 μm). The presence of a solvent leads to an increase of the HOMO-LUMO gap, which changes from 0.5 eV in the gas phase to 1.12 eV (1.11 μm in ethanol [56]. Incoming light from the bottom side is travelling through the glass plate and through

the TCO covered substrate without significant absorption owing to the large band gaps (see Fig. 1.4).

Figure 1.4: Band diagram of a dye sensitized solar cell

As a dye molecule absorbs a photon with an appropriate energy, an electron is excited from the highest occupied molecular orbital (HOMO) to the lowest unoccupied molecular orbital (LUMO). Since both of these levels possess a certain energy width, a continuously spectrum of photon energy can be absorbed.
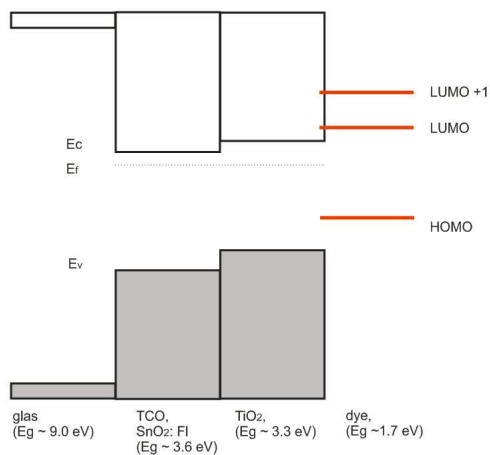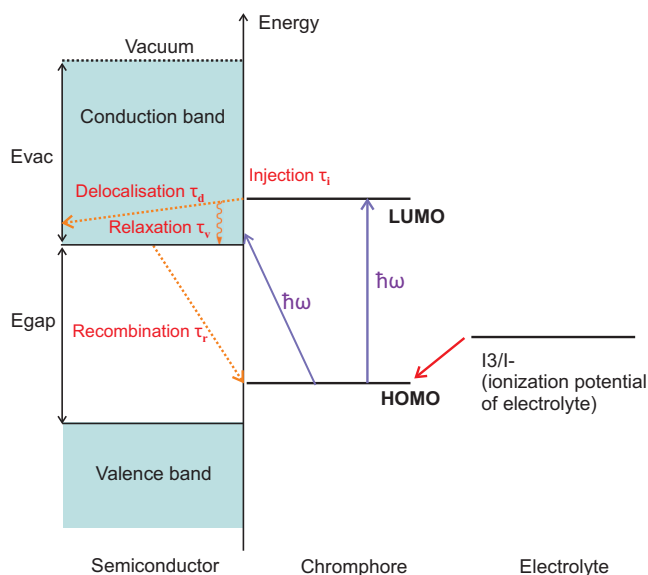

Figure 1.5: Energy diagram of a semiconductor/chromophore interface

The absorption of a photon leads to the existence of an electron hole-pair, which must be separated in order to produce current. The electron is transferred into the semiconductor and the hole in the dye molecule is filled by donations of an electron from a negative ion of the electrolyte solution. The energy alignment of the involved electric levels is here of great importance. The LUMO level must be located above the conduction band minimum for the electron transfer into the semiconductor to occur. The hybridization of the molecular levels (in particular the LUMO) with the substrate can play an important role in the electronic transfer. A LUMO that is highly delocalized over the substrate will allow a fast electron transfer from the dye to the substrate. The ionization potential of the electrolyte-redox pair has to be located above the HOMO level of the dye molecule, in order to refill the hole in the dye molecule by an electron of the electrolyte. The energy alignment is shown in Fig. 1.5. The process of the electron-hole separation occurs for TiO_2 in a timescale on the order of 50 fs and for ZnO in a typical time of 100 ps [7]. The stronger binding and the faster electron transfer from the N3 dye to TiO_2 in comparison to ZnO are possible reasons for the better efficiency of the TiO_2-based over the ZnO-based solar cells. Efficient electron transfer to the conduction band avoids a recombination of the electron with the hole, as well as an energy and voltage loss by relaxation to the bottom of the semiconductor conduction band. [6, 5]

Once the electron leaves the dye molecule, the electron is not trapped on the surface and enters the bulk of TiO_2 [8]. While the electron diffuses through the bulk to the electrode, it relaxes to the bottom of the CB which is thought to occur by vibration coupling. If the electron returns or remains trapped at the surface, it recombines with the positive charge residing on either the chromophore or the electrolyte mediator [14]. When the electron reaches the TCO and travels over the electron circuit to the counter electrode, it meets again the oxidized anion in the electrolyte solution. The chemical reaction for the redox pair I^-/I_3^- to dispense the electron to the dye molecule is $I^- +$

$2h^+ \rightarrow I_3^-$ [4]. With combined UPS and IPS measurements, the electronic levels of the semiconductor and the dye molecule can be determined.

1.2.3   Limiting factors of a DSSC

Recombination of the electron-hole pair is one of the main limiting factors of a DSSC. In this decay channel an electron from the TiO$_2$ interface recombines with the oxidized anion (I_3^-) preventing the photovoltaic process. A strategy to reduce this recombination is to absorb in addition to the N3 molecule an additive like T-Butylpyridine (TBP) on the semiconductor. This is attributed to occupation of bare sites on the TiO$_2$ surface by TBP, limiting the contact between the TiO$_2$ and the electrolyte. [11].

One other approach to reduce the electron-hole recombination rate was to expose a dye covered TiO$_2$ film to a methylsiloxane (CH$_3$SiCl$_3$) vapor in order to cover the patches of TiO$_2$ exposed to the electrolyte. This treatment also reduced the rate of recombination [12].

N3 dye molecules cannot be exposed to the sample surface directly since the required temperature to evaporate the molecules in UHV is higher than its decomposing temperature. Instead, the N3 dye is used in solution with acetonitrile or ethanol as a solvent. In the work described in this thesis, the dye/TiO$_2$ interface was controlled by passivation of the TiO$_2$ surface in UHV, which has the added bonus of protecting the surface from contamination before introducing the sensitization in solution. By sensitizing the surface, the dye molecules replace the pivalic acid ions and a dye/semiconductor interface of high quality is created [47].

1.2.4   Limitations in the arrangement of energy levels:

As mentioned earlier, the peak emission of the sunlight is at a wavelength of 550 nm (2.27 eV). The sun possesses a continuous spectrum of light from infrared to ultraviolet. The power output of an electrical device is defined in general as the product of current

and voltage. The closed circuit current and the open circuit voltage V_{OC} of a DSSC are in competition and both dependent on the energy alignment of the HOMO and LUMO levels of the dye.

The closed circuit current of a solar cell is dependent on the intensity of the incoming light and the absorption spectrum of wavelengths is limited in a DSSC in higher wavelengths. In order to increase the current of a DSSC, the dye molecule should adsorb light with wavelengths up to 900 nm, which can be managed by a decreased HOMO-LUMO gap. The HOMO-LUMO gap cannot be decreased arbitrarily since this energy gap is directly related to V_{OC} of a DSSC. Indeed the V_{OC} of a DSSC is almost given by the potential difference of the CBM and the redox potential of the electrolyte. The choice of the electrolyte in a DSSC is very limited and therefore is the potential of the electrolyte relatively fixed. In order to maximize the voltage, the energy difference between these two potentials has to be as large as possible. To refill the hole in the HOMO level from the electrolyte, the redox potential of the electrolyte has to be located higher in energy than the HOMO. The LUMO level has to be located higher in energy than the CBM to transfer an electron from the dye into the semiconductor. In order to maximize the voltage, the HOMO-LUMO gap has therefore to be as large as possible. Hence, the current and the voltage of a DSSC are in direct competition.

1.2.5 Modifying the N3 molecule

One possibility to change the features of the dye is to add spacer groups between the dye and the surface. By modifying the structure of the dye one can increase physical separation of the cation from the film surface and/or change the reaction energetics and thus the recombination rate. In many instances, additional bridging groups are present, most typically $(CH)_n$ and $(CH_2)_n$, to slow down electron transfer from TiO_2 back to

the chromophore [15], to enhance surface binding, and to improve chromophore stability [14]. With increasing linker length also the electron transfer time from the dye to the semiconductor increases. The distance between the dye and the surface should be modified in a way that the back reaction is minimized without losing efficient electron transfer.

In summary, the main advantage of a DSSC in comparison to traditional Si-solar cells is the economical and simple production with a relatively high efficiency of approximately 10 %. Thus, the DSSC could assert itself on the present market and make solar energy accessible to a broad mass of people. This area of research however is new and requires further intensive studies. One of the most important aspects of a DSSC is the energy alignment of the electronic states of the dye and the semiconductor to each other, since the energy alignment gives information about the open circuit voltage V_{OC} and has strong influence on the electron transfer from the dye to the semiconductor. With the knowledge of the energy alignments steps can be taken to modify the dye molecules systematically to obtain a better efficiency. Efforts were already undertaken to determine the energy alignments of dye/semiconductor systems with UPS- and absorption measurements. Here however, more exact details about the electronic structure in the region of the conduction band are missing and in absorption measurements excitons are always present. [49] Our vacuum chamber is equipped with UPS and IPS systems, which allow studying the electronic structure of a dye/semiconductor interface directly. Besides, with these measurement techniques the presence of excitons are avoided and the measured electronic structure is close to the ground state of the system.

1.2.6 Outline of Thesis

In Chapter 2, a description of the experimental setups of UPS and IPS, as well as other experimental techniques we have used, is given. An insight of the semiconductors (rutile $TiO_2(110)$ single crystal, anatase TiO_2 nanoparticle, $ZnO(11\bar{2}0)$ single crystal, ZnO nanopillar), and the dye molecules (N3, INA, catechol) used in these experiments, as well as previous results from the literature are given in chapter 3. In the fourth chapter the experimental details and the results of the systematic studies are presented. We have measured the electronic level alignment of the three molecules in combination with rutile $TiO_2(110)$ single crystal and $ZnO(11\bar{2}0)$ single crystal. In addition, we studied the electronic structure of N3 dye in combination with an anatase TiO_2 nanoparticle film, as well as with ZnO nanopillars. In the last chapter the results are compared to each other and to results from the literature.

Chapter 2

Measurement techniques

2.1   UltraHigh Vacuum (UHV)

Our sample surfaces are reactive to water and contaminants from the atmosphere. To maintain clean surfaces and to accomplish experiments over a long period of time, an ultrahigh vacuum (UHV) environment is needed. Vacuum is created inside of a stainless steel chamber through a combination of different pumps. Several pumping stages are necessary, since the pumps have different performances for different pressure regions and the pressure difference of an abrupt UHV-atmosphere crossing is too big. The following pumps are used: a rotary vane pump, a turbo molecular pump and an ion pump.

The rotary vane pump is the first step in the pump mechanism and is in direct contact with atmosphere (760 Torr). A schematic diagram of a rotary vane pump is shown in Fig. 2.1(a). The pump creates a low local pressure inside the vacuum chamber by drawning air from the chamber. The rotary vane pump is constituted of a stator and an eccentric rotor which has several vanes (blades) in a diametrical slot. The stator is a steel cylinder, which holds the shaft of the rotor. The axis of the rotor is off center from the stator and the whole of the stator-rotor assembly is submerged in oil. The inlet port is connected to the vacuum system by suitable tubulation usually provided with a dust filter. As a vane passes the inlet port, the vacuum system is connected to the space limited by the stator, the top seal, the rotor and the vane. As the next vane passes the inlet port, the volume of the gas evacuated is isolated between the two vanes. Further rotation sweeps

the isolated gas around the stator, decreases the volume between these two vanes and compresses the gas until the leading vane passes the left exhaust port. The compressed gas is released to the atmosphere and a pressure of about 1 mTorr is produced in the vacuum chamber. The overall compression ratio of the rotary vane pump is 8×10^5 .

The next step to an ultrahigh vacuum is a turbo molecular pump, which is shown in Fig. 2.1 (b). This pump consists of several level static, acute angled stators and acute angled, but movable rotors. The rotors spin with a velocity, which lies approximately in the same magnitude as the mean thermal velocity of the gas molecules and therefore accelerate the gas into the direction of the next stator level. The distance between the levels decreases from level to level and therefore compress the gas further. The factor of compression is approximately five per level and the overall compression ratio is the product of the individual stage ratios. A pump having 9 stages with a compression factor of five should maintain a zero-flow compression ratio of the order $5^9 = 2 \times 10^6$. After the last level the gas is pushed to the outlet and drawn off by the vane type pump. The ability to compress gas is dependent on the type of atoms. Small atoms have high velocities at room temperature and can't therefore absorb much momentum from the rotors. More massive molecules have a small velocity at room temperature and the transfer of momentum from the rotors is much better. Molecular turbo pumps have hence a much worse ability to pump hydrogen in comparison to all other components of air. The great advantage of molecular pumps compared over other pumps that operate in the same pressure range, such as diffusion pumps, is that molecular pumps are free of (hydrocarbon) vapors. Normally the presence of hydrogen, which back diffuses, limits the ultimate pressure to about 10^{-9} Torr. The individual compression ratio of N_2 is $\geq 10^{11}$, of He is 1×10^7 and of H_2 is $\geq 10^5$ [22].

Once a pressure of $\sim 1 \times 10^{-6}$ Torr is achieved, an ion pump can be used. A schematic diagram of an ion pump is shown in Fig. 2.1 (c). An ion pump captures gas molecules
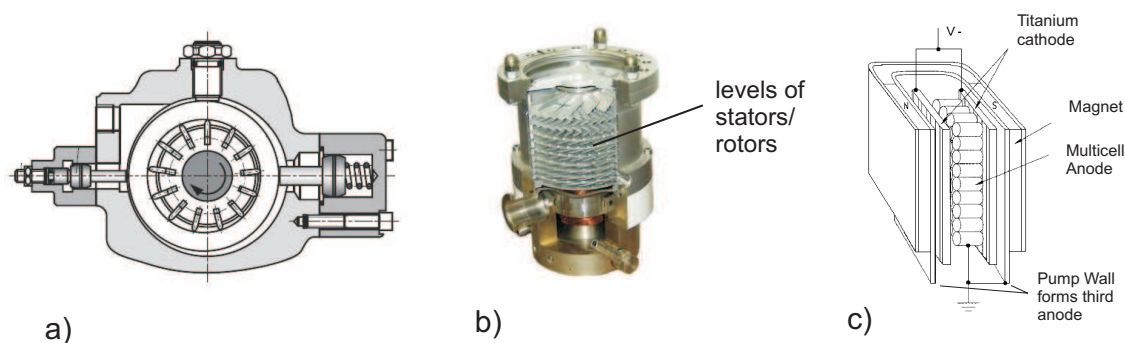
Figure 2.1: a) Schematic diagram of a rotary vane pump (b) cut through a turbo molecular pump (c) scheme of an ion pump

and therefore further decreases the pressure in the vacuum chamber. It consists of two parallel, titanium covered stainless steel walls and an arrangement of stainless steel cylinders, which axes are arranged perpendicular to the walls. Between the two walls a high electrical bias of ~ 6 kV is applied, such that the walls have the function of the cathode and the cylinders the function of the anode. The electrons are emitted from the walls and guided to a spiraled course by a magnetic field of 1500 G, which is directed parallel to the cylinder axes. When the emitted electrons hit the gas molecules, the molecules are ionized and due to the high electric field accelerated to the titanium walls. There, the ionized gas molecules are caught by the titanium by chemisorption. At the impact of the ions on the cathode, titanium atoms are released from the walls, cover the surface of the anode and catch further molecules through chemisorptions. With this method, the pressure decreases to less than 1×10^{-8} Torr. In order to get a pressure of 1×10^{-10} Torr, the water vapor inside of the vacuum chamber has to be removed. The most effective way to get rid of the water vapor is to heat the vacuum chamber for $\sim$24 hours to a temperature higher than 100 °C. Alternatively the chamber can be pumped for approximately one week. After the baking is stopped, the filaments in the vacuum chamber should be degassed. While the walls of the chamber are still warm, the contaminants don't stick immediately on the walls of the chamber and can be disposed by the vacuum pumps. After the chamber has cooled down, it should posses a vacuum environment

($\leq 10^{-10}$ Torr) and be ready for experiments.

2.2   Ultraviolet Photoemission Spectroscopy (UPS)

Photoemission spectroscopy (PS) is based on the photoelectric effect and is used to probe the occupied electronic states of a sample. A monochromatic photon beam is directed onto the sample and electrons are excited out of the sample. The energies of the out coming primary electrons are independent of the intensity of the light and photoemission occurs only when the frequency of the light exceeds a certain minimum. The released electrons are sorted accordingly to their kinetic energy and then captured at the detector which generates an electrical pulse that be recorded as a histogram.

Depending on the energy of the photons, different bands of the material are excited. When using the Kα X-ray emission lines of Al (1486.6 eV) or Mg (1253.6 eV), emission from the core levels of the atoms are accessible. The photons, which are used for ultraviolet photoelectron spectroscopy (UPS) possess a primary energy of 10 to 100 eV and hence induce electron emission of the valence band for most elements. The photons have indeed a penetration depth of up to 1000 Å, but the photoelectrons have a small emission depth of only $\sim$8 Ådue to their strong interaction with the bulk electrons. The region from which primary electrons are emitted in a UPS measurement is therefore restricted to the surface of the sample and thus is very surface sensitive [16].

Photoemission process

The photoemission process can be understood with the help of Figure 2.2. A photon of the energy $h\nu$ is absorbed by an electron and excites this electron from an initial state E_i to an unoccupied final state E_f. If the energy $h\nu$ of the incoming photons is high enough, so that the final energy of the excited electron can overcome the work function,
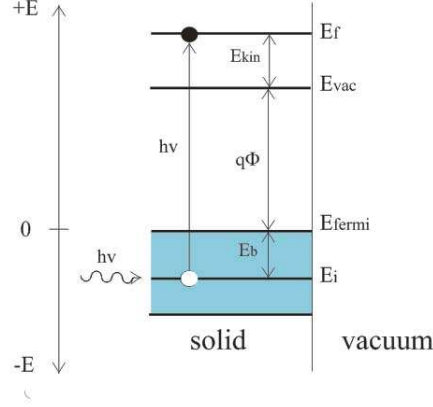
Figure 2.2: Photoemission process for a single electron

the electron can leave the sample and be captured by the detector. The kinetic energy
of the photoelectrons is given by the following equation:

$$E_{kin} = h\nu - E_B - e\Phi, \tag{2.1}$$

where E_B is the binding energy of the electrons in the solid (referred to the Fermi
level) and $e\Phi$ the work function (i.e. the minimum energy required to transfer an electron
to the vacuum level with E_{kin}=0). For the resulting binding energies from the spectra,
the validity of Koopmans theorem is assumed. Koopmans theorem is valid with an ap-
proximation in molecular orbital theory (such as Hartree-Fock theory). The ioniziation
energies are associated with orbital energies and the ionization can be described as the
removal of an electron from a self-consistent field orbital, whereas the other electrons
stay unaffected. Koopmans' Theorem operates under the assumption that the electronic
wavefunction of a multi-electron atom can be described as the Slater determinant of
a set of one-electron wavefunctions (electron correlations are neglected). In addition,
the reorganization of the electrons after the ionization of the molecule is not taken into
account. In many cases, these two energy corrections are of opposite sign and of similar
magnitude ($E_{cor} \approx E_{relax}$). The result of Koopman's Theorem is often close to the real

value, but should be used with care [21].

If the number of photoelectrons is plotted as a function of their kinetic energy, a photoemission spectrum is obtained. The intensity trend of the photoemission curve (arbitrary units) is not only dependent on the occupied electron density N(E), but also on the cross section $\sigma_{abs}(\hbar\omega)$:

$$I(E) \propto N(E - \hbar\omega)\sigma_{abs}(\hbar\omega) \qquad (2.2)$$

To relate $I(E)$ to the DOS of electrons in the solid, the cross section must be known. The photon cross section describes the probability to absorb an electron and is defined by the absorbed energy per time unit, divided by the incoming energy flux. The quantum mechanical coupling between the incoming photons and the initial state is described by the transfer rate Γ, which is known as Fermi's Golden rule (eq. 2.3).

$$\Gamma = \frac{2\pi}{\hbar}(\frac{q}{mc})^2|\langle\Psi_f|\vec{A}\cdot\vec{p}|\Psi_i\rangle|^2\delta(E_f - E_i + \hbar\omega) \qquad (2.3)$$

In this equation the parameter $\vec{A}$ is the vector potential of the incoming light and $\vec{p}$ the momentum operator. The initial state Ψ_i is the wave function of the bound electron state in a solid and the final state Ψ_f is the wave function of a electron in a unoccupied state of the solid. The delta function δ indicates that the transfer can only occur when energy conservation is maintained. To compute the transfer rate, some simplifications and assumptions have to be made. The electromagnetic field of the incoming photon is dealt as a perturbation of the Hamilton ground state of a solid. The matrix element can be simplified by the dipole approximation and the spatial factor of the vector potential of the incoming light $exp(i\vec{k_p}\cdot\vec{r})$ can be reduced to 1. This is acceptable because the wave length of the incoming light λ_p is long in comparison to the lattice spacing of a solid. Thus, the matrix element is reduced to $\langle\Psi_f|\hat{\epsilon}\cdot\vec{p}|\Psi_i\rangle$, whereat $\hat{\epsilon}$ denotes the polarization vector of the incoming light.

With the help of Fermi's Golden rule, an expression for the differential cross section per solid angle can be found (Eq. 2.4). Here, $\vec{k}$ describes the electronic wave vector, ω the angular frequency of the incoming light and $\alpha = \frac{2\pi q^2}{hc}$. The absorption cross section is computed as a function of the incoming electron energy for a given orbital character and is valid for many materials.

$$\frac{d\sigma_{abs}}{d\Omega} = \frac{\alpha|\vec{k}|}{mh\omega}|\langle\Psi_f|\hat{\epsilon}\cdot\vec{p}|\Psi_i\rangle|^2 \tag{2.4}$$
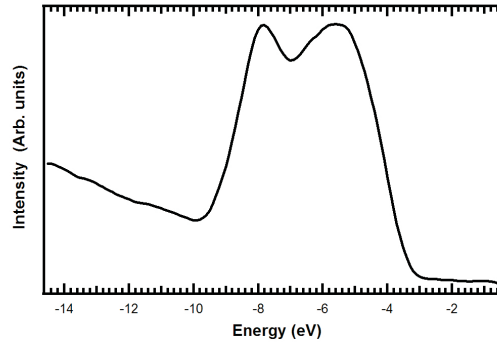

Figure 2.3: UPS spectrum of clean TiO_2 sample.

In Figure 2.3 a valence spectrum of a clean TiO_2 single crystal sample is presented, whereby the energy scale has been rescaled referred to the Fermi level ($E_f = 0$ eV). The valence band consists mostly of states with O $2p$ character. The valence band maximum (VBM) can be determined by linear extrapolation of the band edge and leads to a value of -3.3 eV. Again, the shape of the curve is proportional to the DOS times the cross section.

Experimental

The photon source of our UPS spectrometer is a helium discharge lamp. Helium gas is pumped through a lamp and an electric arc excites the He atoms. Photons generated by the decay of these atoms are directed through a thin quartz cylinder onto the sample. These photons have well defined energies. A He I photon has an energy of 21.2 eV and

is given by an electron decay from a hybridized 1s2p to a 1s state. A He II$_\alpha$ photon has an energy of 40.8 eV and is given by an electron decay from a $2p_{3/2}$ or a $2p_{1/2}$ to a 1s state of a single ionized He atom. The He II$_\beta$ line has an energy of 48.4 eV and can be neglected due to its small intensity. The ratio of intensity from discharge of He II$_\alpha$ to He I increases with decreasing helium pressure in the lamp.
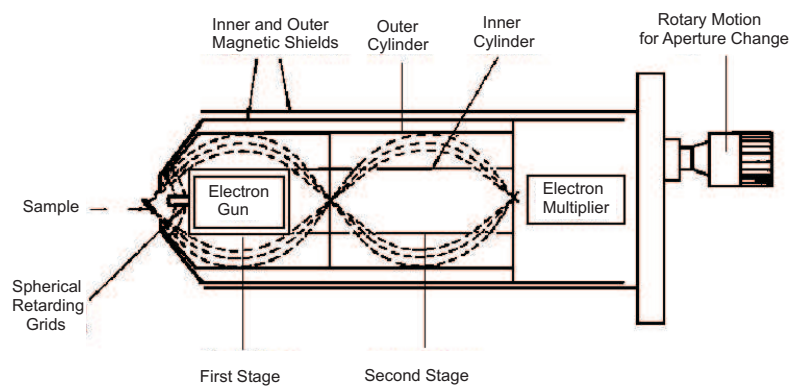
Figure 2.4: Schematic design of a Cylindrical Mirror Analyzer

In our measurements, photoelectrons are captured by a cylindrical mirror analyzer (CMA) and analyzed in regard to their kinetic energy. A schematic diagram of the CMA is shown in Figure 2.4. The CMA consists of two coaxial metal cylinders. Putting different biases on the two cylinders, an electric field is generated and only electrons within a narrow energy range are able to get through an arrangement of slits. When the electrons are too fast or too slow, they strike one of the two metallic cylinders. Varying the applied bias changes the kinetic energy of the electrons that successfully pass through the cylinders, and those electrons are detected and counted by the electron multiplier.

When a photo emitted electron impacts the entrance of the channeltron electron multiplier (CEM) an avalanche of $\sim 10^7$ electrons is generated through secondary electron emission. The resulting pulse is easily detected with standard amplifying electronics and allows a counting of primary particles. The CEM consists of one insulating glass
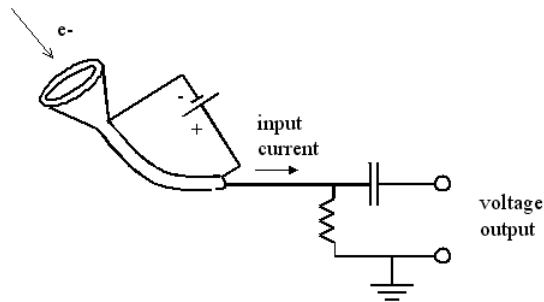
Figure 2.5: Schematic diagram of a channeltron electron multiplier

tube, where the inner surface is covered with a high-resistance SiO_2 layer. Between the cathode at the open end of the tube and the anode at the closed end, a bias (typically 3 kV) is applied, which generates an electric field along the axis of the glass tube. When the primary electrons hit the inner wall in the region of the cathode, several secondary electrons are released, accelerated through the existent electric field and release in turn additional electrons. The result is a measurable electron cascade.

A side effect, which occurs inside of the CME, is that positive ions are accelerated into the direction of the cathode. If they strike near to the cathode, secondary electrons would also cause an electron cascade and create a false signal. This ion feedback effect is effectively prevented by a circular or helical bended glass tube of the CEM. Due to the bigger mass, the ion trajectories enclose a much bigger angle to the line of electric flux parallel to the axe of the tube. The route of the ions is thereby short, the energy small and secondary electrons are hardly produced. Furthermore, the distance between the point of the impact and the anode is small, and thus the resulting avalanche effect is smaller.

The CMA, which schematic diagram is shown in Fig. 2.4, is operated in the retarding mode. The retarding mode acts as a high pass filter, as the electrons are slowed down through two hemispherical grids in front of the entrance of the analyzer. The hemispherical grid, which is closer to the sample, is grounded and no electric field exists in the space between the sample and the CMA. A bias is applied to the second grid, so that

the kinetic energy of electrons is reduced and only electrons with enough kinetic energy are able to reach the analyzer. At the analyzer, as discussed earlier, the electrons are filtered and counted in regard to their kinetic energy.

The resolving power of the energy analyzer is E/ΔE, where E is the energy of the electrons reaching the detector, in this case the pass energy, and ΔE is the energy range of electrons reaching the detector, also known as the energy resolution. The resolving power is fixed by the geometry of the system. Thus, reducing the pass energy will improve the energy resolution of electrons reaching the detector, which is commonly described as increasing the resolution the analyzer. The majority of UPS measurements were taken in this work with a pass energy of 15 eV, for which the energy resolution is ~0.1 eV. [23]

Energy calibration

At the beginning of this chapter, the problem of how to define the binding energy in respect of the Fermi energy of the semiconductor material was discussed. At first, we should remember the equation to determine the kinetic energy (Eq. 2.1).

The kinetic energy of the electrons depends on the energy of the incoming photons, the binding energy of the electrons before excitation and the material specific work function. For all measurements of photoemission spectra, the sample is in thermal equilibrium with the sample holder, the detector and the vacuum chamber. Thus, the level of the Fermi energy is the same for the sample and for the detector. The photon energy used in UPS measurements is equal for all experiments.

To calibrate the energy, a spectrum of the metal Au is taken. The spectrum of the Au sample is shown in Figure 2.6.

In this Au-spectrum, which is plotted as intensity as a function of kinetic energy, the electrons with the highest kinetic energy have their origin at the Fermi level, in which case $E_B^m = 0$. The kinetic energy corresponding to the electrons from the Fermi level can be
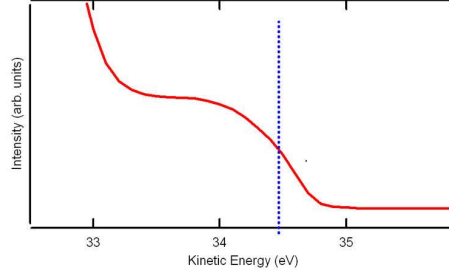
Figure 2.6: UPS spectra of Au (intensity vs energy). The vertical line marks the kinetic energy of electrons coming from the Fermi level.

determined with the support of the Fermi-Dirac statistic and the location of the inflection point. We obtain the value $E_K^F = 34.5$ eV and have therefore a reference point for all further measurements. With this achieved data, the energy scale of the electrons can be converted into a binding energy scale. When the general equation $(E_K = h\nu - E_B - q\Phi)$ is subtracted from the equation for the metal $(E_K^m = h\nu - E_B^m - q\Phi)$ and as reference point the Fermi Energy $E_K^m = E_K^F = 34.5$ eV with $E_B^m = 0$ is chosen, following result is gained:

$$E_B = 34.5 \text{ eV} - E_K \tag{2.5}$$

2.3 Inverse Photoelectron Spectroscopy (IPS)

Emission process

In contrast to UPS, in inverse photoelectron spectroscopy (IPS) electrons of a well defined kinetic energy are directed towards the sample and the emitted photons are detected. The electrons penetrate the sample with a finite probability and couple to unoccupied states of high energy. A fraction of these electrons decay into unoccupied states of lower energy and emit a photon. The process is presented in Figure 2.7.
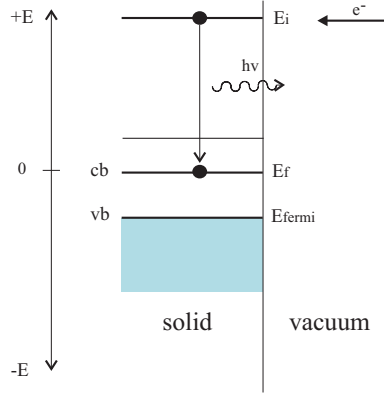
Figure 2.7: Schematic diagram of the inverse photoemission process.

The energy difference between the initial state E_i and the final state E_f is equal to the photon energy. When the level of the initial state is defined, conclusions about the final state can be drawn by the measurement of the intensity as a function of energy. The number of detected photons is proportional to the unoccupied density of states of the material, as well as to the cross section of absorption of the unoccupied states. Once again, Fermi's Golden rule describes the electron transfer rate of from the initial to the final state. In inverse photoemission spectroscopy the outgoing electromagnetic fields have to be quantized. The expression for the differential cross section per solid-angle, derived from Fermi's Golden rule, is shown in equation 2.6. When we compare this expression with the one of the photoemission (Eq. 2.7), whereby we assume that the matrix elements are identical and the electron and photon energies typical of those in these studies are 20 eV and 40 eV respectively, we obtain an interesting result. The ratio of these two values is in the magnitude of 10^{-5}, viz. that the cross section of the IPS is much smaller than that of the UPS. Since the incident particle rate is higher for IPS than for UPS, the total ratio of the count rates is respectively about 10^{-2}. To obtain spectra with a good signal to noise ratio, the IPS data must be collected over a longer period of time.

$$\frac{d\sigma}{d\Omega_{em}} = \frac{\alpha\omega}{mc^2 h|k|}|\langle\Psi_f|\hat{\epsilon}\cdot\vec{p}|\Psi_i\rangle|^2 \qquad (2.6)$$

$$\frac{d\sigma_{IPS}}{d\Omega}/\frac{d\sigma_{PS}}{d\Omega} = (\frac{\lambda_e}{\lambda_p})^2 \qquad (2.7)$$

Experimental

The IPS can be used in two different ways: in the isochromate mode and in the spectrograph mode. In the so-called isochromate mode, the incoming electron energy is varied and the photons emitted at a fixed energy are measured. In the spectrograph mode, which is used in the measurements presented here, the energy of the incoming electron is fixed and a grating dispersed photon is detected in parallel on 2-D micro channel plates. With this method, a better focus of the electron beam onto the sample is possible and the measurement stays stable for a long period of time. The design of the grating spectrometer is based on the Rowland circle, with utilization of the focusing and dispersion attributes of a concave spherical mirror with grooves. A simple grating spectrometer is shown in figure 2.8. If the emanating point of photons is located somewhere on the Rowland circle with radius R, the scattered beam is focused to other points on the same circle in all orders. The grating mirror possess a curvature of a radius $R_m = 2R$, so twice the radius of the Rowland circle. The grating of our system has a line spacing of 1200 lines/mm and a radius curvature of 750 mm. By determining the location of the scattered point conclusions can be drawn of the wavelength and thus of the energy of the emitted photons. This is illustrated in Fig. 2.8 (a) where rays composed of wavelength λ_1 and λ_2 are shown to undergo such diffraction and focusing.

The figure shows a ray emanating from a point source A, hitting the grating, and being diffracted and focused back onto the Rowland circle. The rulings run parallel to the z-axis which will be referred to in this discussion as the vertical direction. The dispersion direction lies in the xy-plane and is called the horizontal direction. A further
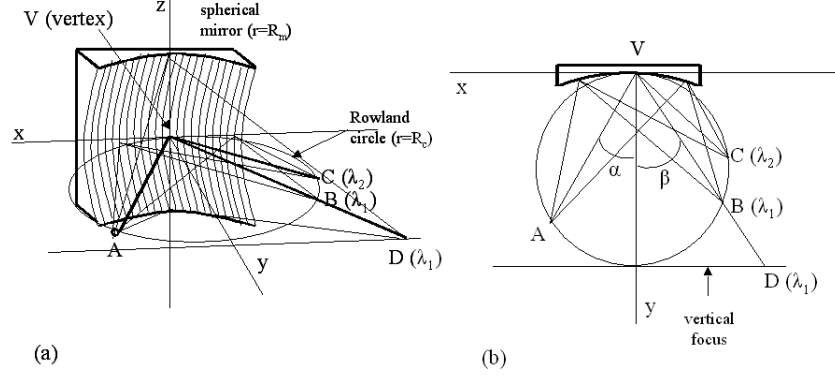
Figure 2.8: Schematic diagram of the properties of a spherical mirror with verttical grooves, the Rowland circle is in the xy-plane

attribute of the spherical mirror is astigmatism. Rays that propagate in the horizontal xy-plane with wavelength λ_1 and strike the grating will be focused on the circle in point B. Rays with the same wavelength, which have also a z-component in their propagation, are focused along a vertical line that passes through point B. It is important to note that two rays emanating from the same point with the same wavelength λ_1 will be focused along the same vertical line that passes through point B. The horizontal component of the dispersed ray is only dependent of its wavelength and gives therefore definite information about its energy.

Rays near the z = 0 diffraction can be described by the following equation which is the grating equation for a concave grating:

$$\pm m\lambda = d(sin\alpha + sin\beta) \tag{2.8}$$

α and β are the angles of incidence and reflectance, respectively. In this equation, the choice of the positive sign describes the situation where the image lies between the grating normal and the specular (i.e. the line defined by $\alpha = \beta$), otherwise referred to as inside order. The choice of negative sign refers to outside order, where the image lies

outside the specular.

Another important quantity, the linear dispersion, is given by:

$$\frac{d\lambda}{dl} = \frac{d cos\beta}{mR} = \frac{cos\beta}{mR(1/d)} \times 10^4 /mm \qquad (2.9)$$

where l is a distance measured along the detector. It is important to point out that the final resolution of the instrument will be a result of both the optical resolution, which is approximated by equation 2.9, and the energy spread of the electrons in the electron source, which is in our case about $1mm^2$. Figure 2.9 shows the configuration of our grating spectrometer in the UHV system. The detector can be moved along the Rowland circle and detect the dispersed and focused light of the spherical grating.
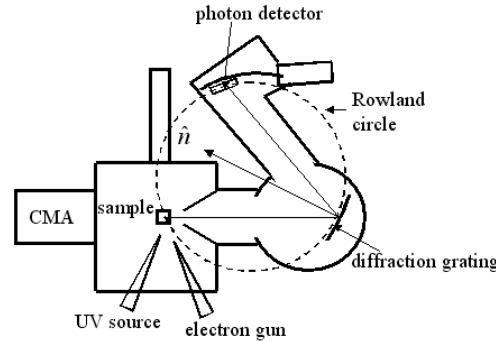

Figure 2.9: Schematic arrangement of the grating IPS and PS system inside of the vacuum chamber.

After the photons are dispersed and reflected as a function of their energy by the grating mirror, they are detected by a 2D-detector. The 2D-detector converts the photon into a measurable electron signal and signal processing electronics send the position of the incoming photons to the data acquisition computer. The detector, which is shown in Fig. 2.10, consists of two micro channel plates and a resistive anode encoder. The micro channel plate consists of an arrangement of straight, small, continuous dynodes. When a photon hits the upper micro channel plate, a group of electrons is generated.

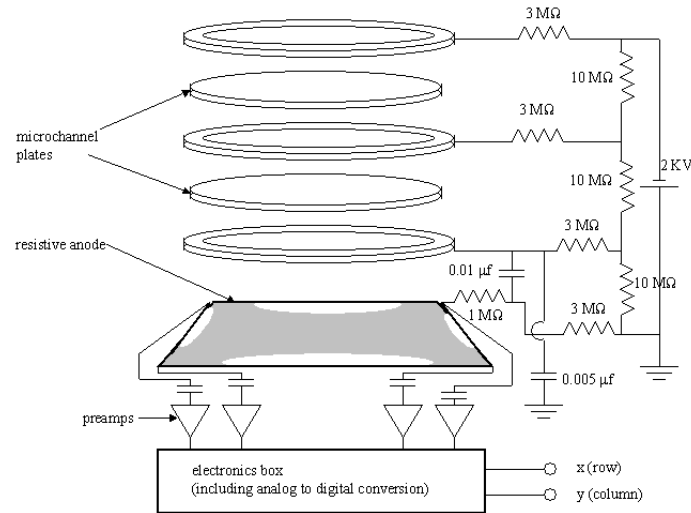These electrons are accelerated by an applied electric field through the plate and out of the bottom side.

Figure 2.10: Schematic arrangement of the photon detector

When the electrons reach the second plate, every electron releases in turn its own group of electrons, which are accelerated again through the plate in direction of the anode. The anode consists of a sheet of uniform resistance. When the electrons hit the anode, a charge is distributed and collected at each corner of the film. The magnitude of the charge from each corner of the sheet gives information about the location of the signal, so that each electron impact can be associated with coordinates. The computer saves the coordinates of the events as two 8-bit numbers, or more exactly as an array of the size 256 x 256. In this photon current array, the row coordinate is along the Rowland circle and indicates the particular photon energy. The column coordinate corresponds to the vertical unfocused photons, which are produced by the astigmatism of the grating mirror. These unfocused photons have, as discussed earlier, all the same photon energy. All photons with the same row coordinate can therefore be added within a column and as result a one-dimensional histogram of the energy distribution can be gained. The row positions are evenly spaced and can be calibrated by a comparison spectrum of a clean metal. At a metal, the unoccupied states start directly at the Fermi level, which is again

chosen as the reference point. Thus the position of the initial state is known due to the photon energy, the photon energy scale can be converted to a electron energy scale by the relation $E_f = E_i - h\nu$.
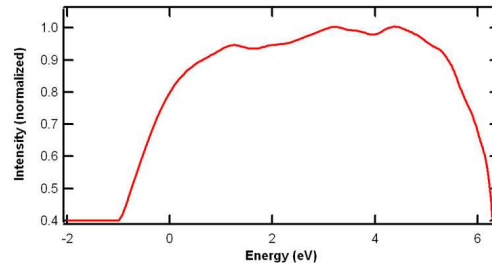

Figure 2.11: Spectrum of the aperture function. Photons of uniform intensity are detected in a 20-37 eV range, whereby the energy is scaled in regard to the Fermi level.

To consider the whole instrument aperture into an acquired spectrum, a detector function is taken. Electrons with a kinetic energy of 40 eV are directed onto a Au sample. Since Au has no features whithin the detection range of 20-37 eV, the out coming photons have an uniform intensity. Fig. 2.11 shows the spectrum of these photons with uniform intensity. The detector registers apparently more photons between 1 and 5 eV, and less photons beyond. To normalize the measured spectra, they are divided by this detector function.

2.4 Scanning Tunneling Microscopy (STM)

The scanning tunneling microscope scans the surface of a sample with a tungsten tip in a raster movement and creates a topographic/electronic image of the surface. If the tip is only a few nanometers away from the surface, the wave functions of the electrons in the tip and the wave functions of the electrons at the surface of the sample start to overlap. Once a bias between the STM tip and the sample is applied, electrons tunnel between the tip and the surface. The sign of the bias determines in which the direction the electrons are tunneling. An electronic feedback system regulates the height of the tip in regard to

the sample surface. Since the magnitude of tunnel current depends exponentially on the distance between the tip (see Eq. 2.10), this measurement technique is very sensitive to distance changes.

$$I \propto V \rho_s(0, E_f) e^{-2\kappa z} \qquad (2.10)$$

The measured tunnel current is depending on the local density of states $\rho_s(0, E_f)$, which is located near the Fermi level, on the applied bias V and on the distance z to the object. The parameter κ quantifies the decay of the waves inside of the barrier [20].

There are different ways of scanning the surface. In the mode of constant height, the absolute height of the tip above the sample is not varied. With the measurement of the tunnel current a 3-dimensional image of the object can be created. This is only possible for very flat surfaces, because a danger of collision of the tip and object exists. The advantage of this mode is that a very quick raster scan of the sample surface maybe obtained. With the mode of constant current, the height of the tip to surface is continuously varied by change the voltage on a piezoelectric ceramic on which the tip is mounted and the measured tunnel current is kept constant. An electronic control system is responsible for the continuous regulation of the distance. This electronic control system measures in a loop procedure the current and changes the height of the tip accordingly. Since the tip/system still possess a small motion due to vibrations, heat and oscillations, it is difficult to obtain a constant current. When the current comes close to the correct value, the height of the tip isn't corrected any more and an average of the present current is taken. The obtained 3-dimensional image corresponds to the local density of states in combination with the topography of the surface. The advantage of this method is that a very high spatial resolution can be achieved, so that the atomic electronic structure of the surface maybe visible. The measuring rate however is limited by the electronic control system, and the generation of an image takes several minutes.

In this work, the images have been taken in the constant tunnel current mode.

As the principle of scanning tunneling microscopy is based on the measurement of the current flow between tip and sample, only electric conductive samples, such as metals or semiconductors, can be studied directly.
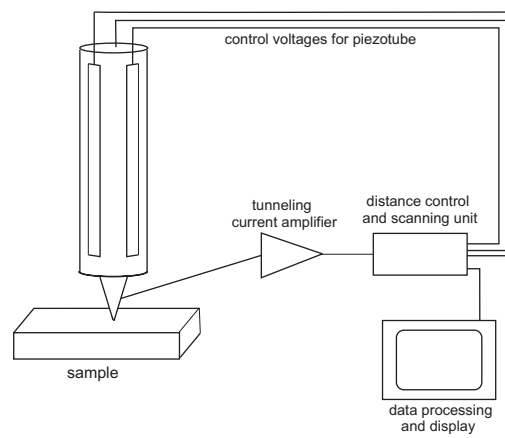

Figure 2.12: Schematic arrangement of the STM

Due to the very small distance between tip and sample surface of $\leq$ 1 nm, the scanning tunneling microscope has to be isolated from vibrations. This is achieved with a combination of spring-and-damping system. Furthermore, fluctuations in the temperature have to be avoided, since deformations and changes of lengths in the system cause drift. Also an electromagnetic shielding towards the environment is required by reason of the very small tunnel currents. To protect the sample against contamination, the experiments are performed in a vacuum environment of 2×10^{-10} Torr.

2.5 Auger electron spectroscopy

Auger electron spectroscopy is used to identify elements in the region of the surface and to make a rough statement about their quantity. In this technique, a monochromatic beam of electrons of 3 keV energy is directed onto the sample. Electrons from the beam

collide with the electrons from the solid and holes in the core region of the atoms are left behind. These holes are refilled with electrons of higher energy states and the excess energy is released either in form of X-ray photon or by emission of a third, so called, Auger-electron (see fig. 2.13).
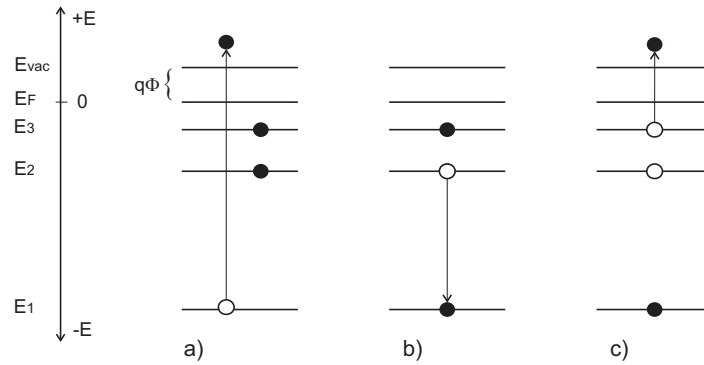

Figure 2.13: Principle of the Auger process: (a) Emission of a core electron (b) Refilling of the hole by an electron of a higher energy state (c) Energy transfer and emission of a third electron.

The kinetic energy of the Auger electron is defined only by the characteristic energy levels of the target atom, and is independent of the kinetic energy of the incoming electrons.

$$E_k = (E_1 - E_2) + E_3 - q\Phi \tag{2.11}$$

Upon energy analysis of emitted electrons, element specific maxima are found in the lower energetic region (50-2000 eV). Due to the small energies of the Auger electrons, the mean free path is relatively short (typically 10 Å) and the method is surface sensitive.

In our AES measurements, an electron gun contained in a CMA produces the electron beam, and the CMA collects and energy analyzes the electrons emitted from the sample. As with UPS, electrons of a specific kinetic energy are selected by the voltages applied to the inner and outer cylinders. In AES, however, the CMA is not operated in retarding

mode, so no retarding voltage is applied to the grid at the entrance aperture, and only the voltage of the outer cylinder is varied, while the inner cylinder is grounded. In this mode, a higher current of electrons reaches the detector, including a large amount of inelastically scattered electrons.To make the features from Auger electrons stand out more strongly, a voltage modulation technique is emplyed to measure the first derivative of energy distribution of the emitted electrons (dN(E)/dE). For a CMA, this quantity is proportional first derivative of the collector current (I(E)) [24].

2.6 Low Energy Electron Diffraction (LEED)

Low energy electron diffraction (LEED) is used to determine the symmetry of a surface. An electron beam of low, but well defined energy (50-200 eV), is directed onto the sample and elastically scattered electrons are detected by a fluorescent, phosphorus coated screen. If the surface contains a well ordered, periodic surface, a diffraction pattern with sharp glowing points will be visible. The diffraction pattern is an image of the reciprocal 2-D lattice of the surface, from which conclusions can be drawn from the surface structure of the crystal.
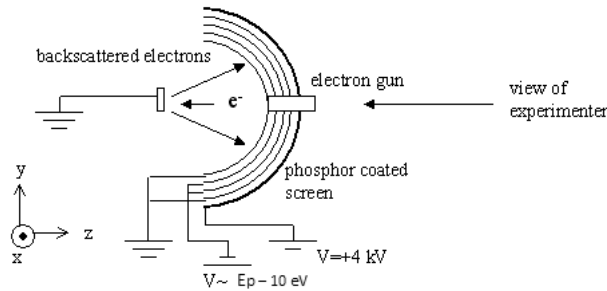

Figure 2.14: Schematic diagram of a LEED experiment

In Fig. 2.14 a schematic diagram of a LEED experiment is presented. The detector consists of four concentric stainless steel mesh grids and a phosphor coated screen. The first grid is grounded to circumvent electric fields in the region of the sample. The task of second and third grid is to reject inelastic scattered electrons from the screen. A negative

bias is applied to these two grids, which is only slightly lower than the kinetic energy of the incoming electrons. Inelastic scattered electrons don't possess enough energy to overcome this potential and are therefore kept away. The usage of two grids makes the repulsive field more homogeneous and is mechanically more stable. To avoid electric fields near the screen, the fourth grid is grounded again. A voltage of +4 kV is applied to the phosphorus coated screen, which is installed behind these four grids. As soon as electrons are getting near to the screen, they are attracted by this positive bias. The areas which these electrons strike, begin to fluoresce and their positions, symmetry, and pattern can be determined .

The penetration depth of the incoming electrons is approximately 10 Å due to their low energy. This permits the approximation of the surface lattice as a two dimensional structure. The real lattice vector $\vec{r}$ and the reciprocal lattice vector $\vec{g}$ are related by following equation:

$$\vec{r_i}\vec{g_j} = 2\pi n \delta_{ij} \tag{2.12}$$

From the condition of constructive interference in an electron diffraction experiment it emerges, that the wave vector of the incoming electron $\vec{k}$ and of the back scattered electron $\vec{k}'$ must differ by a surface reciprocal wave vector $\vec{G}$. The reciprocal wave vectors can be determined by Fourier transform of the real wave vectors, whereby the symmetry of the real and the reciprocal space are identical. Eq. 2.14 follows from the condition of the elastic scattering $|\vec{k}| = |\vec{k}'|$.

$$\vec{k} - \vec{k}' = \vec{G} \tag{2.13}$$

$$|G| = 2\left|\vec{k}\right| sin\theta = 2 \cdot 2\pi/\lambda \cdot sin\theta \tag{2.14}$$

The parameter λ describes here the wavelength of the incoming electrons and θ the scattering angle.

Chapter 3

Materials: Semciconductor and Dye

For a better understanding of the physical processes in a DSSC, the semiconductors TiO_2 and ZnO, as well as the molecules N3, INA and catechol are introduced. Afterwards, model calculations and experiments from the literature of the dye N3 and catechol absorbed on TiO_2 are shown.

3.1 Semiconductor

In contrast to metals, semiconductors have a band gap separating the valence band and the conduction band. In this region, no electronic states are present. Different measurement techniques are available to determine the value of a semiconductor band gap. In optical absorption spectroscopy, the absorption of a photon excites an electron from the valence band (VB) to the conduction band (CB). To first order, the photon energy, where the onset of absorption occurs, is equal to the energy band gap of the semiconductor. The electron-hole interaction however modifies this energy to lower values. The electron and the corresponding hole are attracted to each other by the Coulomb force and this electron-hole pair is called exciton. In UPS/IPS measurements, no electron-hole pairs are generated and the real transport band gap can be determined. The value of the transport band gap is greater than the value of the optical band gap.

3.1.1 TiO$_2$ and TiO$_2$ samples

Titanium dioxide has a broad range of applications. To name only a few examples, it is used in heterogeneous catalysis, as a photo catalyst, as gas sensor, as white pigment in cosmetic products and in electric devices such as varistors [26]. TiO$_2$ is able to endure repeated photo excitation and is chemically stable in various environments. Furthermore, titanium dioxide is a wide band gap semiconductor, non-toxic, easy and inexpensive to produce.

TiO$_2$ crystallizes in three major structures: rutile (tetragonal, $a = b = 4.58$ Å,$c = 2.953$ Å), anatase (tetragonal, $a = b = 3.78$ Å, $c = 9.50$ Å) and brookite (rhombohedral, $a = 5.44$ Å. $b = 9.17$ Å, $c = 5.14$ Å). However, only rutile and anatase play any role in the applications of TiO$_2$ and are here of interest. A schematic diagram of the rutile and anatase bulk structure is shown in Fig. 3.1.

Bulk structure

The unit cells of rutile and anatase TiO$_2$ are shown in Fig 3.1. In both structures, the basic building blocks consist of a titanium atom surrounded by six oxygen atoms in a more or less distorted octahedral configuration. In anatase, the corner-sharing octahedral form (001) planes. In both TiO$_2$ structures, the stacking of the octahedron result in threefold coordinated oxygen atoms. Since titanium-oxide has many stable chemical phases with a variety of crystal structures, TiO$_2$ can be reduced easily. Bulk reduction and the resulting color centers are reflected in a pronounced color change of TiO$_2$ single crystals from initially transparent to light and dark blue. The bulk structure of reduced TiO$_{2-x}$ is quite complex with a various types of defects such as doubly charged oxygen vacancies, Ti^{3+} and Ti^{4+} interstitials, and planar defects. The defect structure varies with oxygen deficiency which depends on temperature, gas pressure, impurities, etc. These intrinsic defects result in n-type doping and high conductivity, which allows
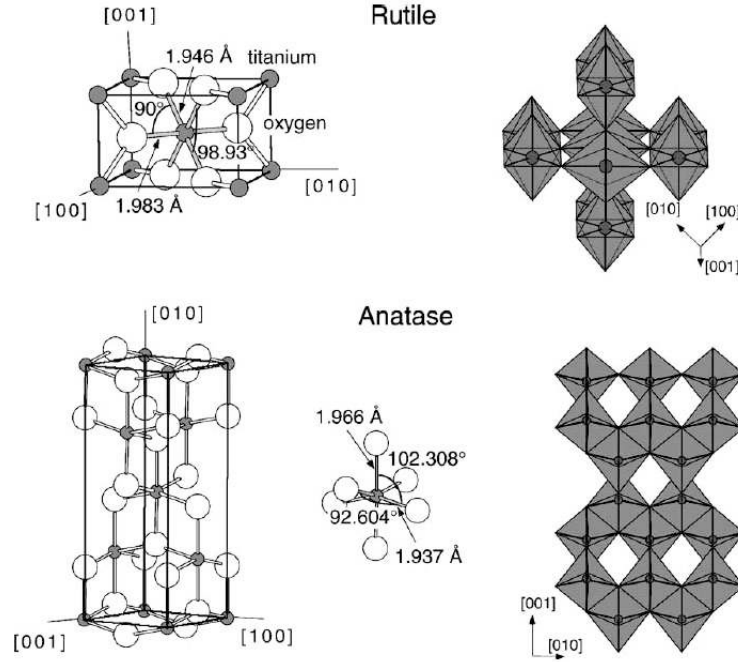
Figure 3.1: Bulk structures of rutile and anatase. The tetragonal bulk unit cell of rutile has the dimensions, a = b = 4.587 Å, c = 2.953 Å, and the one of anatase a = b = 3.782 Å, c= 9.502 Å. In both structures, slightly disordered octahedron are the basic building units. The bond lengths and angles of the octahedrally coordinated Ti atoms are indicated and the stacking of the octahedron in both structures is shown on the right side. [26]

spectroscopic and STM measurements to scan the surface [26].

For rutile, the (110) surface is the most stable. With the Wulff construction, one can determine the form of a crystal in thermodynamic equilibrium, whereby the free energy of the surface is minimized. The Wulff construction in Fig. 3.2 shows that in anatase crystals the only two surfaces exposed to the vacuum are the (101) and (001) surfaces. The anatase (101) surface is the most stable one. Calculations of surface energies of the relaxed structures indicate that the average surface energy of an anatase crystal is lower than that of a crystal in the rutile phase. This could explain the fact that, experimentally, TiO_2 nanoparticles are found to prefer a less stable anatase structure for diameters
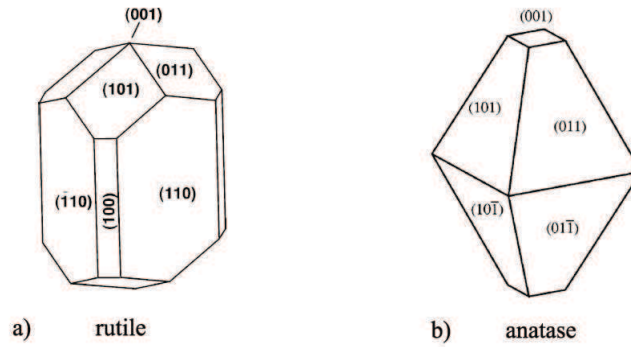
Figure 3.2: The equilibrium shape of a TiO$_2$ crystal in (a) rutile [31] and (b) anatase [32] form using the Wulff construction and the calculated surface energies.

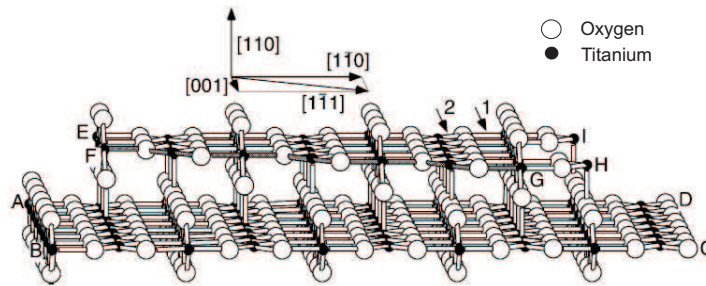up to about 10 nm [33].

Rutile (110) surface

Figure 3.3: The structure of the relaxed rutile stoichiometric (110) surface. [26]

Although the rutile (110) surface is the most stable crystal face, it nevertheless reconstructs and restructures at high temperatures under both oxidizing and reducing conditions. The rutile (110)-(1x1) surface in Fig. 3.3 contains two different kinds of titanium atoms. Along the [001] direction, rows of six fold coordinated Ti atoms (as in the bulk) alternate with fivefold coordinated Ti atoms, with one dangling bond perpendicular to the surface. Two kind of oxygen atoms are present as well. Within the main surface plane, they are threefold coordinated as in the bulk. The so-called bridging oxygen miss one bond to the Ti atom in the removed layer and is twofold coordinated.

These bridging atoms are thought to be removed easily by thermal annealing, because of their coordinated under-saturation.

Anatase (001) and (101) surface

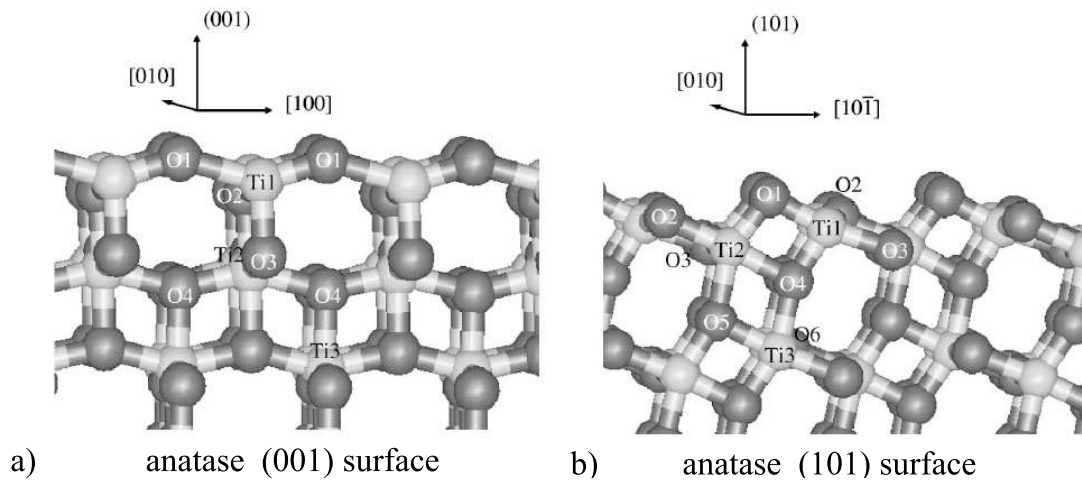a)   anatase (001) surface   b)   anatase (101) surface

Figure 3.4: The structure of the relaxed anatase stoichiometric (a)(001) (b) (101) surface. Equivalent atoms have the same label. [32]

On the (001) surface of anatase, which is shown in Fig. 3.4 (a), fivefold-coordinated Ti atoms are present (denoted Ti1), as well as twofold- and threefold-coordinated oxygens (O1 and O2, respectively). In the relaxed surface, the mirror plane symmetry along the [100] direction is broken: the two O1-T1 bonds become strongly inequivalent, with bond lengths of 2.20 and 1.76 Å.

The anatases (101) surface, which is shown in Fig. 3.4 (b), is very corrugated with a characteristic sawtooth profile perpendicular to the [010] direction. On it, both fivefold- and sixfold-coordinated Ti-atoms are present (denoted Ti1 and Ti2, respectively), as well as twofold and threefold oxygens (O1 and O2, respectively). Each bridging oxygen (O1) is bonded to one Ti1 atom and one Ti2 atom [32].
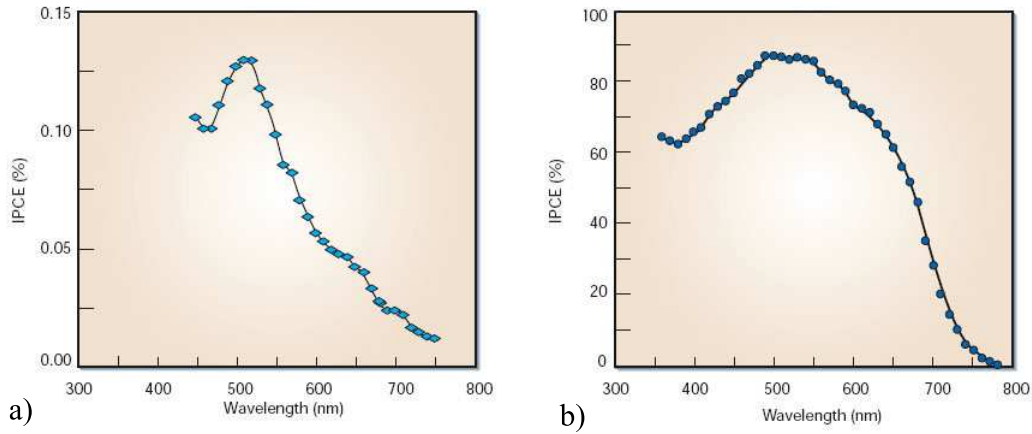
Figure 3.5: The nanocrystalline effect in dye-sensitized solar cells. In both cases, TiO_2 electrodes are sensitized by the N3 dye. The incident-photon-to-current conversion efficiency is plotted as a function of the excitation wavelength. (a) Anatase (101) single crystal (b) nanocrystalline anatase film [2].

We used rutile (110) single crystals and anatase nanoparticle films for our studies. The rutile TiO_2(110) single crystal possesses a relative flat and simple structure and is thus convenient for physical processes studies. The size of a anatase nanoparticle on the TiO_2 films, which were used in this work, is about 12-15 nm. The films are grown on a fluorinated tin oxide (FTO) glass substrate by spin coating and are annealed afterwards at $\sim 450°C$ for 30 minutes.

The incident-photon-to-current conversion efficiency (IPCE) spectrum of a dye / semiconductor system is a good indicator how effective the system will be in a DSSC. In this measurement technique, light of a certain wavelength is directed onto a DSSC with corresponding substrate. The wavelength of the incident light is increased stepwise and the efficiency of the DSSC is detected. In Fig. 3.5, the ICPE of anatase single crystal is compared to the ICPE of anatase nanoparticles. Anatase nanoparticle samples have shown a seven times greater IPCE than single crystal samples and are therefore a better suited for DSSCs. This striking improvement is due largely to the far greater surface area of the dye-sensitized nanocrystalline film as compared with a flat single-crystal electrode,

but is also due, at least in part, to the mesoscopic film texture favouring photogeneration and collection of charge carriers the mesoscopic film texture favouring photogeneration. The TiO$_2$ nanoparticle sample has a light harvest which is a factor of 1000 greater than the single crystal sample. [2]

The incident-photon-to-current conversion efficiency (IPCE) is plotted as a function of wavelength.

3.1.2 ZnO and ZnO samples

Zinc oxide has attracted a significant amount of attention in the past several years since this wide band gap semiconductor finds a number of applications in catalysis, gas sensing, and the fabrication of varistors and other microelectronic devices.

From a physical/chemical point of view, ZnO is a very interesting material because of the mixed covalent/ionic aspects in the chemical bonding. ZnO crystallizes in the hexagonal Zn and O planes stacked alternately along the c-axis (see Fig. 3.6 (a). Anions and cations are fourfold coordinated, respectively, like in the closely related zinc-blende structure. Wurtzite crystals are dominated by four low Miller index surfaces: the non-polar ($10\bar{1}0$) and ($11\bar{2}0$) surfaces and the polar zinc-terminated (0001)-Zn and oxygen terminated ($000\bar{1}$)-O surface (see Fig. 3.6 (a)). Density-functional studies from B. Meyer and D. Marx show that the nonpolar surfaces have much lower surface energies than the polar surfaces [36]. Oxygen vacancies in the bulk behave like donor states and make the undoped, reduced sample to a n-type semiconductor.

The stoichiometric ZnO($11\bar{2}0$) surface consists of Zn and O chains, whereby each zinc atom is bound to two oxygen atoms at the top layer, and to two oxygen atoms at the second layer. The coordination of the surface atoms is reduced from fourfold to three-fold, thereby creating an occupied dangling bond at the anion and an empty dangling bond at the cation. A model of a ZnO($11\bar{2}0$) surface is shown in Fig. 3.6 (b) [37]. The
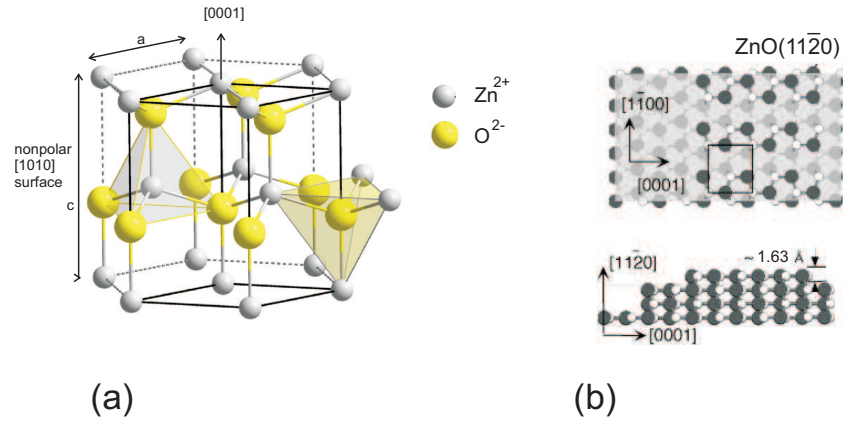
Figure 3.6: a) Wurtzite structure of ZnO (a = 3.250 Å, c = 5.207 Å) (b) model of a ZnO(11$\bar{2}$0) surface from top and side view [37].
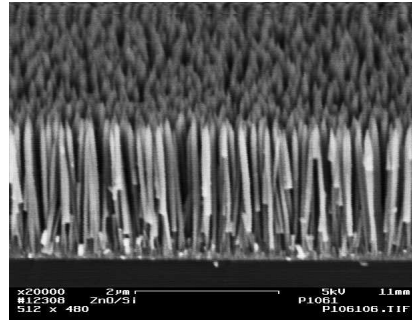
unit cell is 5.21 Åwide and 6.50 Ålong.

Figure 3.7: Image of a typical ZnO nanorod structure.

We use (11$\bar{2}$0) single crystals and nanopillar films for our studies. The ZnO(11$\bar{2}$0) single crystal single crystal possesses a relative flat and simple structure and is thus convenient for physical processes studies. Nanorods are grown by metalorganic chemical vapor deposition (MOCVD) at relatively low temperatures. This method ensures a uniform grow, which leads to a small density of defects, a uniform size and orientation of the nanorods [41]. Solar cells with ZnO-nanorods (ZnO-n) have shown similar efficiencies to solar cells with ZnO colloidal nanoparticles (ZnO-c), but hold a greater potential. The electrons in the nanorod don't have to overcome any grain boundaries and possess high

transport mobility due to the single crystal structure. Experiments have shown a photo to current reaction time of ~ 30 μs [35], which is about two orders of magnitude faster than for the ZnO-c samples. For a perfect single crystal, the total transfer time can be extrapolated to 1μs. The life time of the electrons in the semiconductor is similar for both structures. The difference in the surface area plays only a minor role, though ZnO-c has a roughness factor far greater than ZnO-n (roughness factor is the ratio of the real surface area and the geometrical surface area). From these facts it can be concluded that the recombination rate for ZnO-n during electron transportation is very small, if not even negligible [42].

Zinc-collodial solar cells show at present an efficiency of 5 % [35].

Our ZnO nanorod samples grown on a silicon substrate, have a length of 1.8 μm and a diameter of 100 nm. The ratio of length to diameter is therefore 18.

3.2 Dye

In DSSCs, the dye molecule is responsible for the optical features of the system - it facilitates absorption of light in the solar spectrum. A good overlap of the energy levels between the lowest unoccupied molecular orbital (LUMO) of the dye and the conduction band of the semiconductor, as well as a mixing of these energy levels, are important factors to initiate a fast electron transfer into the conduction band of the semiconductor. The requirements to the dye molecule are stability in ground- and oxidized-states, and to endure repeated oxidations and regenerations. Electron transfer from the excited dye to the semiconductor should process as fast as possible to decrease the recombination rate with the corresponding hole.

3.2.1 N3-Dye

Ruthenium complexes with polypyridine ligands have been shown to have a good performance in DSSC's and the N3 molecule is one of the most efficient dyes [57]. N3, or more

precisely Ru(4,4-dicarboxylate-2,2-bipyridine)$_2$-(NCS)$_2$, possesses two biisonicotinic acid and two thiocyanate (NCS) ligands. Its structure is shown in Fig. 3.8. The carboxyl group (COOH) is the anchor group, with which the molecule binds to a semiconductor surface.
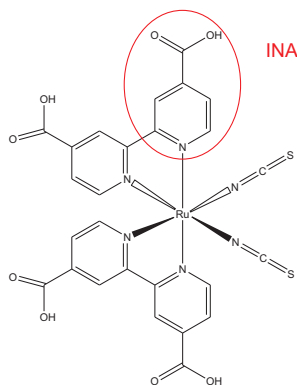

Figure 3.8: Structure of the N3 molecule

According to theoretical calculations, the HOMO of the N3 molecule is localized around the Ru atom and along one thiocyanate chain, while the LUMO is delocalized around one of the bipyridine ligands (see Fig. 3.9) [27].
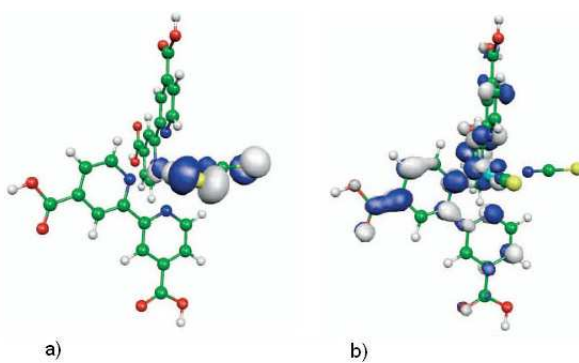

Figure 3.9: Spatial distribution of the (a) HOMO and (b) LUMO of unbound N3 dye [27]

3.2.2 Isonicotinic acid (INA)

The isonicotinic acid (INA) molecule consists of a pyridine ring and of a carboxylic acid group (see Fig. 3.10). As seen from the circled ligand in Fig. 3.8 it is a part of the larger N3-dye molecule and can be considered as the analog to the N3 linker. While the attributes of this molecule should not be exact the same as the attributes of the pyridine/carboxyl ligands of the N3 molecule, some similarities could still exists in bonding behavior and in the LUMO level. According to calculations, the excited state of the INA molecule is very delocalized at room temperature and the electron transfer to TiO_2 occurs in a time interval of 4.9 fs [46]. The isonicotinic acid molecule was studied absorbed on $TiO_2(110)$ and $ZnO(11\bar{2}0)$ single crystal surfaces.
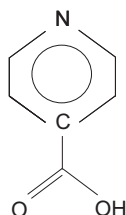
Figure 3.10: Structure of the isonicotinic acid molecule. INA is the analog to the N3 linker.

3.2.3 Catechol

The catechol molecule is one of the smallest organic sensitizing chromophores. It consists of a benzene ring and two hydroxyl groups (see Fig. 3.11). Catechol can be used as an anchoring group for the dye molecules used in DSSC and has recieved particular attention because its binding to TiO_2 is stronger than any other type of anchoring group. Another advantage of catechol in comparison to carboxylate groups is that now slow desorption in the presence of water takes place, which may limit the long-term stability of the solar cell. [54] It has shown that the molecule lowers the absorption threshold of TiO_2 significantly [51]. The spatial distribution of the HOMO and LUMO of free catechol is shown in Fig. 3.12.
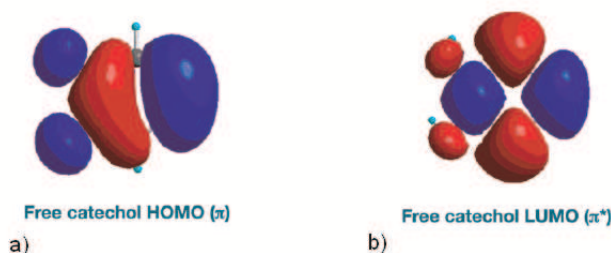
Figure 3.11: Structure of the catechol molecule

Free catechol HOMO (π)

Free catechol LUMO (π^*)

a)

b)

Figure 3.12: Spatial distribution of the (a) HOMO and (b) LUMO state of the unbound catechol [52]

3.3 Dye-surface interface

3.3.1 N3/TiO$_2$

Bonding configurations

N3 has four carboxyl (COOH) groups that could bind in several ways either by molecular or dissociative adsorption [50]. This leads to a number of possible configurations by which the N3 molecule might bond to a TiO$_2$ surface. Several binding studies agrees with each other that the most probable binding configuration is through one COOH group where the carboxyl group loses a H atom and bridge bounds to two Ti atoms (see Fig. 3.13 (a)). Other binding possibilities of the carboxyl groups to titanium are shown in Fig. 3.13 (b) and (c) [47].

Spatial distribution of the HOMO and LUMO

It is believed that the dye molecule binds by two pyridine/carboxyl-acid ligand to the semiconductor TiO$_2$. According to calculations for the electronic structure from

a) bidentate bridging
(dissociative)

b) bidentate chelating
(molecular)

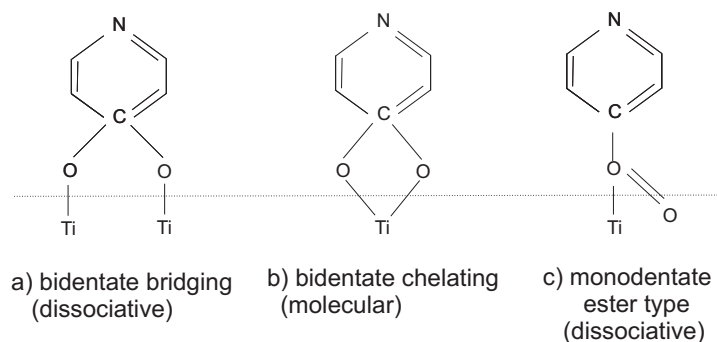c) monodentate
ester type
(dissociative)

Figure 3.13: Binding configurations of the N3 dye to TiO_2: (a) bridge binding (b), (c) less probable binding configurations.

Persson and Lundqvist [48], the LUMO of the N3 dye is located at one of the two pyridine/carboxyl-acid ligands, which binds to TiO_2. Fig. 3.14 represents the spatial distribution of (a) HOMO and (b) LUMO in connection to an anatase TiO_2 cluster. The lines represent the bindings between the atoms, and the blue and white features represent the orbitals of interest. In connection with TiO_2, the LUMO orbital is not restricted to the dye molecule, but mixes in this model to 14 % with the conduction band of TiO_2. This mixture of the spatial distribution leads to an efficient electron transfer to the TiO_2 semiconductor. Between the HOMO of N3 and the conduction band of TiO_2 no mixture exists.
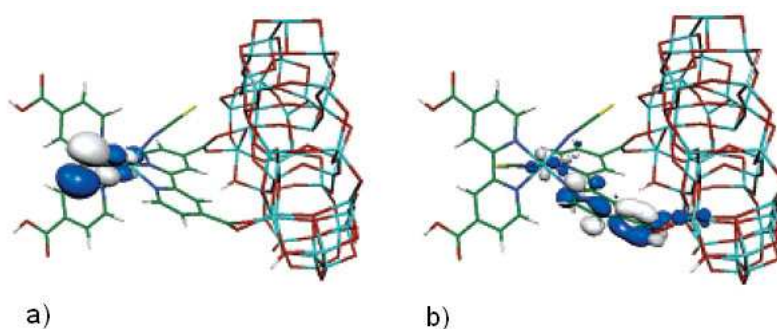

a)   b)

Figure 3.14: Calculated spatial distribution of the (a) HOMO- and (b) LUMO-level of N3 bond to anatase $TiO_2(101)$. [48]

Band bending

As a n-type semiconductor, TiO_2 might create in contact with dye molecules a negative charged surface area by trapping electron at the surface. To maintain electric neutrality, a layer of positive charges is formed inside of the semiconductor, which shifts the electrostatic potential and bends the energy band upwards to higher energies. The agglomeration of charges creates a Schottky barrier against incoming electrons [14]. With combined UPS and IPS measurements it is possible to identify the energy shifts and to relate the energy levels correctly to each other.
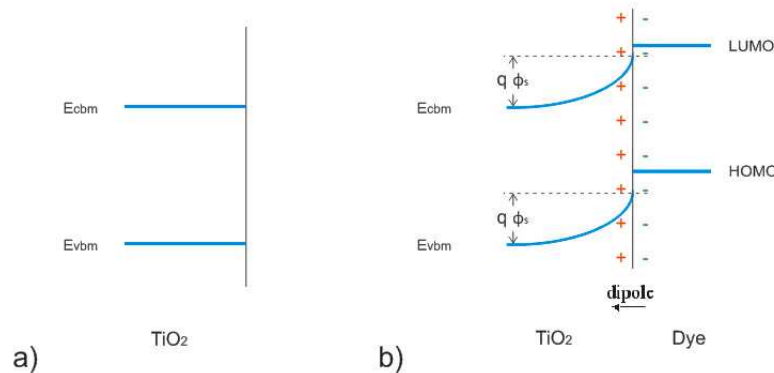

Figure 3.15: a) Band diagram of TiO_2 (b) band diagram of TiO_2 in connection with N3-Dye, the bands are bend upwards due to the dipole.

3.3.2 Catechol/TiO_2

Catechol provides two hydroxyl groups for binding to a semiconductor. The catechol/TiO_2 interface offers some interesting features in the electronic structure and in electron transfer dynamic. Research groups constrain their previous models and calculations to catechol/anatase TiO_2 systems and give only indications, but no solid background to our catechol/rutile TiO_2 experiments [51] [52] [53]. Nevertheless, a comparison is helpful.

Duncan and Prezhdo have performed optical absorption measurements on free and bound catechol (anatase $TiO_2(101)$) molecules [52]. The spectra of their optical absorption measurements are shown in Fig. 3.16. Compared to the spectra of free catechol,
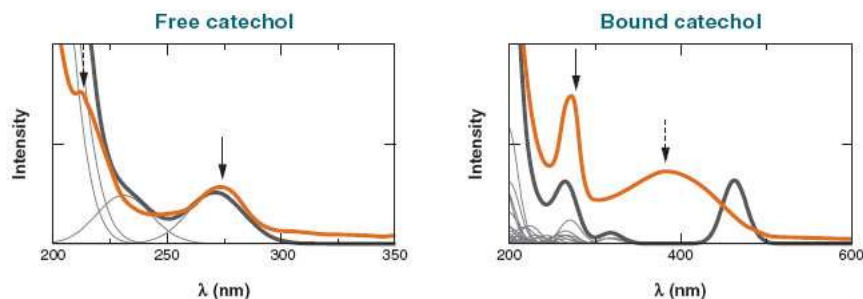
Figure 3.16: Experimental (orange line) and theoretical (grey line) spectra of free cat-echol (left side) and bound catechol (right side). For the bound catechol an additional energy band appears, which comes from the very strong energy coupling to TiO_2. [52]

the spectra of bound catechol possess an additional absorption band at 420 nm. The wavelengths of the transition from the HOMO to the LUMO of free catechol in the region of 270 nm can be still observed in bound catechol. The lowest energy band of the free catechol is present at a wavelength of 300 nm. According to their calculations, the new energy band appears due to a direct charge transfer from the catechol into the semi-conductor. A schematic diagram of this process is represented in Fig. 3.18, scheme 2. This is caused by a strong electronic interaction between the catechol and the semicon-ductor. Fig. 3.17 shows images of the HOMO and LUMO orbitals, which are involved in the dominant transitions of free and bound catechol. The orbitals are taken from Hartree-Fock (HF) calculations. The bound HOMO and (LUMO+8) are very similar to the HOMO and LUMO of the free catechol. The (LUMO+2), which consists mostly of a d-orbital, gives the biggest contribution for the new low energy band at 380 nm for the titanium bound catechol.

Persson, Bergström and Lunell have done some calculations for catechol in connection with anatase TiO_2 nanoparticles [51]. The calculations were performed by the interme-diate neglect of differential overlap (INDO) model, parameterized for spectroscopy at the configuration interaction (CI) level of theory. According to their view, the (LUMO+1)
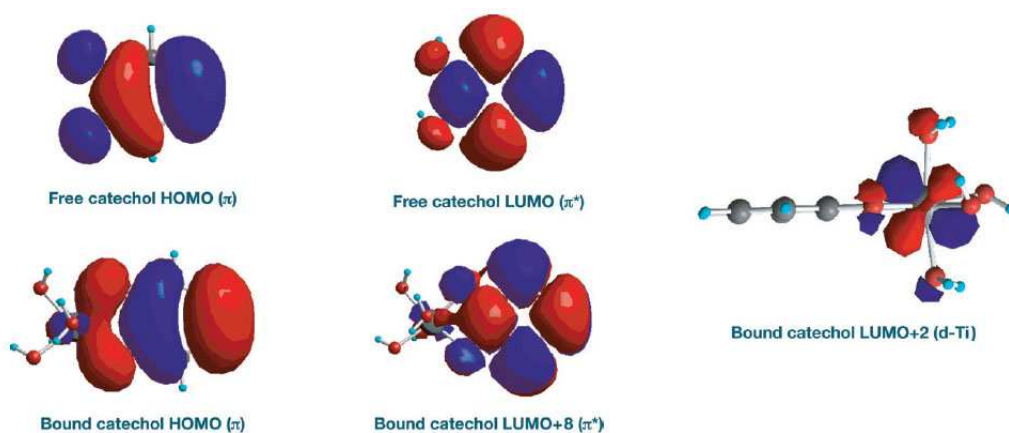
Figure 3.17: Images of the key orbitals of catechol in free state and bound to hydrated Ti^{4+} ion in solution. The highest occupied molecular orbital (HOMO) of free catechol matches the HOMO of the bound system. However, the lowest unoccupied molecular orbital (LUMO) of free catechol matches the LUMO+8 of bound catechol. The LUMO of bound catechol and several orbitals above the LUMO are localized on titanium and are responsible for the new low-energy optical band [52]

orbital is localized deep inside of the TiO_2 cluster. By photo excitation, the electron is transferred directly from the HOMO of he catechol into the conduction band of the semiconductor. The excitation energy is hereby 420 nm. In the DOS of the bound system, the first LUMO contributions of the catechol are estimated 3 eV above the CBM. There are further interactions in higher energy regions with the conduction band, but they are in general smaller than for (LUMO+1).
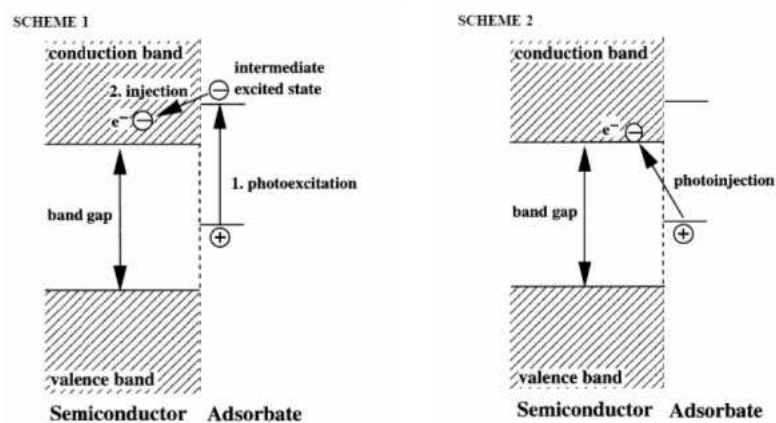
Figure 3.18: Mechanism of the electron transfer from catechol to the semiconductor TiO$_2$. Scheme 1: indirect transfer, Scheme 2: direct transfer. [52]

Chapter 4

Experimental details and results

4.1 Experimental details

4.1.1 Equipment of the vacuum chamber

We performed our experiments in two different vacuum chambers. In the first vacuum chamber, a UPS and IPS system are used for measurements of the valence and conduction bands. In addition, a CMA, a UV source, a X-ray source and an electron gun are present. The second vacuum chamber posses a STM, with which topographic-electronic images can be taken. Both vacuum chambers are equipped with Auger and LEED systems, which allow a check of the purity and the quality of the surface structures. In addition, both vacuum chambers are connected to a load lock used as a preparation chamber, in which the samples can be quickly transferred in and out of the chamber. The base pressure in the main chambers is about $5\text{x}10^{-10}$ Torr, the base pressure in the preparation chambers is about $2\text{x}10^{-9}$ Torr.

4.1.2 Sample preparation

In order to measure the energy level alignment between adsorbate and substrate, clean and adsorbate covered surfaces have to be prepared and then to be studied with the combination of UPS and IPS measurements.

We studied several different adsorbate/substrate combinations. As substrates we used rutile $TiO_2(110)$ single crystal, anatase TiO_2 nanoparticle film, $ZnO(11\bar{2}0)$ single
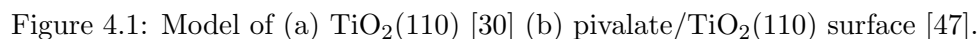
crystal and ZnO nanorods grown on silicon. As adsorbates we used N3 dye, isonicotinic acid and catechol.

The TiO_2 and $ZnO(11\bar{2}0)$ single crystals were cleaned by sputtering with 1 kV Ar^+ ions for 20 min and subsequently annealing at a temperature of $\sim 630 - 680$ °C and $\sim 540 - 590$ °C, respectively, for 15 min. The purity of the sample was determined by Auger spectroscopy and the quality of the surface structure by LEED measurements. To free the TiO_2 nanoparticles from water, the sample was annealed for one hour at a temperature of approximately 200 °C. The ZnO nanorods were also annealed for one hour at 350 °C.

The surface cannot be exposed to a gas of N3 molecules in UHV since the required temperature to evaporate the molecule in UHV is higher than its decomposing temperature. The N3 molecule cracks before it can be evaporated onto the surface. The N3 dye is in solid state form and can be placed in solution with ethanol or acetonitrile as solvent. The semiconductor/TCO/glass sample is placed into the N3 solution for $\sim$10 min minutes and the N3 dye molecules completely cover the surface. Subsequently, a rinsing with pure solvent removes the additional, unbound molecules from the surface. One has to be careful not to put the zinc oxide samples into the N3/solvent solution for a too long time (≥ 1 h), otherwise complex formation between ZnO^{2+}-ions and the sensitizer takes place [45]. Absorption of INA onto the surface was also performed by dissolving the molecule in acetonitrile and dipping the substrate into the solution.

To protect the clean sample surface as it is transported in air to the adsorbate solution, a passivation of the surface with pivalic acid was performed. Pivalic acid is a solid with sufficiently high vapor pressure to be used for dosing the sample. It is stored in a glass tube, which is connected by valves to the load lock of the STM vacuum chamber. After the glass tube is purged of water vapor by several freeze-melt cycles, the sample is exposed to $1x10^{-6}$ Torr pivalic acid for 100 seconds.

Catechol is a liquid at room temperature and can be exposed to the sample surface in the same procedure as for INA. It is stored in a glass tube, which is connected to the load lock of the UPS/IPS vacuum chamber and covers the sample surface with a self limiting monolayer.

4.2 Dye/TiO$_2$ results: STM images and Electronic Level Alignment

4.2.1 STM images of N3/TiO$_2$

Figure 4.1: Model of (a) TiO$_2$(110) [30] (b) pivalate/TiO$_2$(110) surface [47].

We used STM imaging to monitor the preparation of N3/TiO$_2$(110) surface. The STM images shown in this section were taken at a tip bias of -2.0 eV, and a constant current between 0.5 nA and 1.0 nA. This bias corresponds to tunneling into the unoccupied states of the sample.

To be able to interpret the STM images of rutile TiO$_2$(110) single crystal, it is good to know its surface structure. In Fig. 4.1 (a) a model of the rutile TiO$_2$(110) single crystal surface is shown. The white balls in this figure represent Ti-atoms and the dark shaded balls represent O-atoms. This choice of color was made in order to getter better comparison with the STM images, since in the images the titanium atoms appear generally bright. The oxygen atoms at the surface are drawn darker than the oxygen atoms in the bulk. The rectangle indicates the unit cell of a (1x1) structure. The four six

fold coordinated Ti-atoms at the corners are covered by bridge oxygen atoms and only the Ti-atom in the center (fivefold coordinated) is visible. The unit cell is 6.5 Å x 3.0 Å. With lines outlined one can recognize a distorted hexagon in figure 4.1, which connects four fivefold coordinated and two six fold coordinated Ti atoms. The dimension of this structure is 6.5 Åin length (one unit cell) and 6.0 Åin width (two unit cells) [30]. The model in Fig. 4.1 shows how the pivalate ion binds to the $TiO_2(110)$ surface.

(a) clean TiO_2(110)   (b) pivalate covered TiO_2(110)
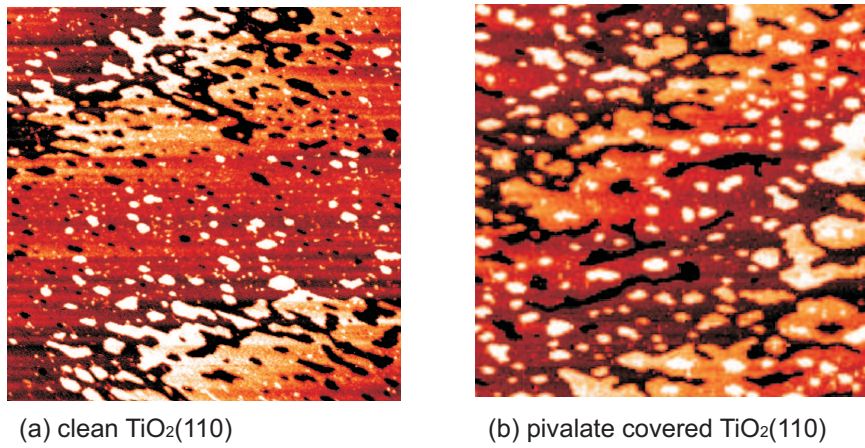
Figure 4.2: (200 x 200) nm scanning tunneling microscope images of (a) clean and (b) pivalate covered rutile TiO_2(110) surface.
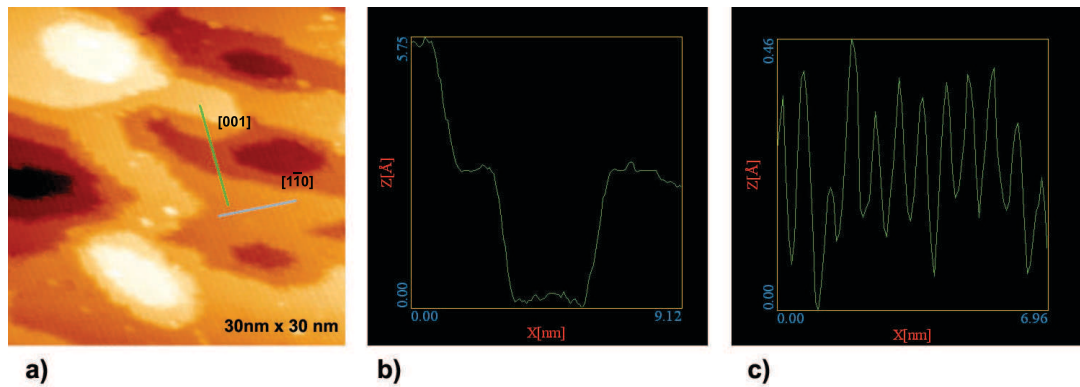

Figure 4.3: (a) Scanning tunneling microscope image of clean and rutile TiO_2(110) surface (30 nm x 30 nm), (b) height profile in [001] direction, (c) height profile in [$1\bar{1}0$] direction.
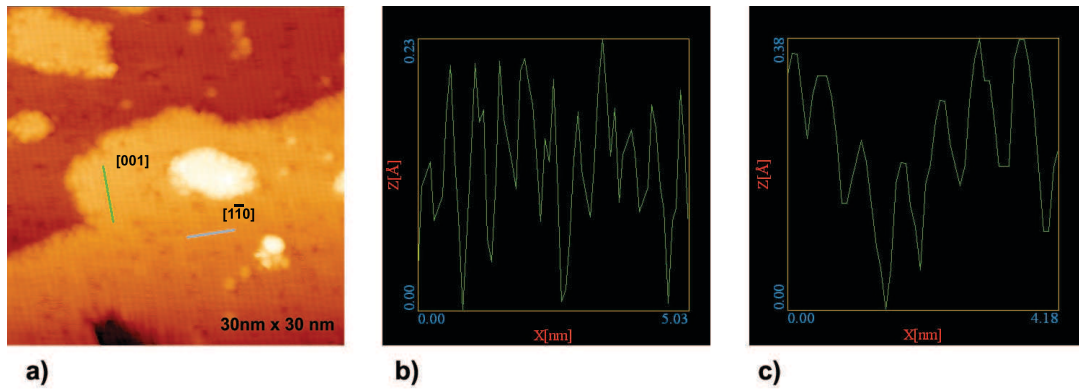
Figure 4.4: Scanning tunneling microscope images of pivalate covered rutile $TiO_2(110)$ surface (30 nm x 30 nm), (b) height profile in [001] direction, (c) height profile in [1$\bar{1}$0] direction.

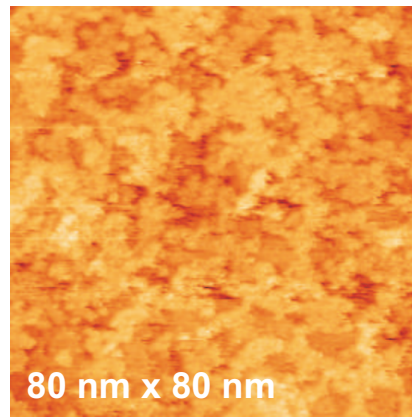

Figure 4.5: Scanning tunneling microscope images of dye covered rutile $TiO_2(110)$ surface (80 nm x 80 nm).

In figures 4.2 (a) and (b) STM images with a resoulution of (200 x 200) nm of a clean and of a pivalic acid covered TiO_2 surface are shown. On the clean surface, large flat terraces (up to 1000 Åin extent) are observable. By comparing both images, it can be observed that the structure of the pivalate layer conforms to the structure of the substrate, which is in agreement with with work of Sasahara et al. [47].

Fig. 4.3 (a) shows a STM images of a clean $TiO_2(110)$ surface with a lower resolution of (30 x 30) nm. The alternating bright and dark rows give a indication for the (1x1) structure, as they are presented in the model shown in Fig. 4.1 (a). A height profiles

was taken along the [001] and along the [1$\bar{1}$0] direction. In the height profile along the [001] direction, the step height of the terraces can be determined to be (2.9±0.4) Å, which is in agreement with the literature value of 3.2 Å[28]. In the height profile along the [1$\bar{1}$0] direction, the distance of the Ti-rows can be examined. The obtained distance of the Ti-atoms is (6.1±0.5) Å, which also agrees well with the literature value of 6.5 Åpredicted in the model in Fig. 4.1 (a).

The surface was then passivated with pivalate ions, and imaged again, as shown in Fig. 4.4. The bright spots in this image represent pivalate ions that form a monolayer which fully covers the TiO$_2$(110) surface. With the height profiles along the [001] and the [1$\bar{1}$0] direction, the distance of the pivalate ions to each other can be determined. The pivalate molecules are separated in the [001]-direction about (6.2±0.7) Å, in the [1$\bar{1}$0]-direction about (4.6±0.5) Å. The pivalic acid molecules bind to the TiO$_2$ surface in a regular and ordered way and protect it well from contamination in the atmosphere. To verify this statement, the passivated surface was brought to the atmosphere and transferred back again into the vacuum chamber. The STM images before and after the transfer show the same terrace width, step density and step height and indicate therefore that the surface didn't change.

After sensitization of the surface in a N3/acetonitrile solution, a STM image was taken of the fully covered N3/TiO$_2$(110) surface, as shown in Fig. 4.5. The morphology of the surface structure is again maintained and has endured different environments (pivalic acid, atmosphere, acetonitrile, N3 dye) very well. The dye molecule covers the surface area-wide and leaves nothing visible of the original substrate.

4.2.2 N3/rutile TiO$_2$(110) single crystal

The electronic level alignment of the dye/TiO$_2$ system is determined by UPS and UPS measurements, by comparing spectra from the clean and subsequently the dye sensitized surface.
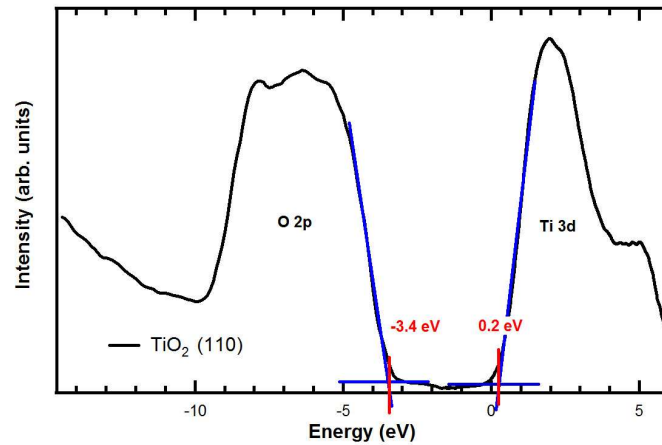

Figure 4.6: Linear fitting procedure of band edges for a TiO$_2$(110) single crystal surface.

In Figure 4.6 a UPS/IPS spectrum of a clean TiO$_2$(110) single crystal surface is presented. The valence band is composed mostly of states with O $2p$ character, which is located between $\sim$ -11 eV and $\sim$ -3 eV. The conduction band consists primarily of states with Ti $3d$ character. The CBM is located close to the Fermi level. To determine the band gap, the edges of the valence and conduction band are extrapolated by a linear fit. These fits are shown as straight lines in the figure. The illustration shows a spectra of a rutile TiO$_2$(110) single crystal sample, which edges are determined to be -3.4 and 0.2 eV.

Fig. 4.7 presents a UPS/IPS spectrum of the clean and the dye covered TiO$_2$(110) surface. The curves clearly show visible differences. Since a coverage of one monolayer of dye molecules is estimated, it is assumed that the thickness of the sensitized layer is about the diameter of the dye molecule (10 Å). The measurement techniques UPS and IPS possess due to the similar electron energies a similar surface sensitivity. The
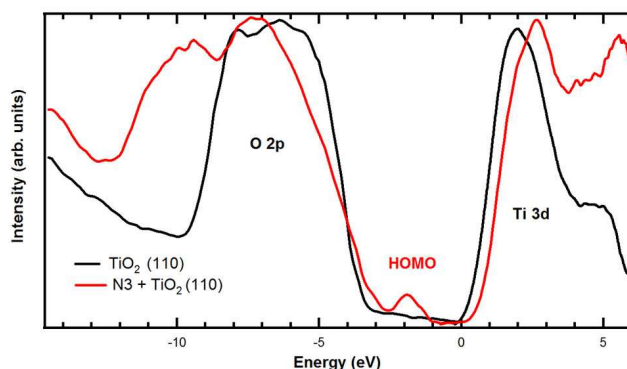
Figure 4.7: UPS and IPS spectra of the clean and dye covered TiO$_2$(110) surfaces.

energy of the electron for UPS is in the region of 20-35 eV, whereas the electrons for IPS measurements possess energy of about 20.3 eV.

After sensitization of the surface, a clear contribution of the N3 molecule can be observed in the region of the TiO$_2$ band gap, which is is commonly referred as the HOMO. Also a shift of 0.6 eV for the CB is observed for the spectral features. The most likely explanation for this shift is that a dipole is created at the dye/TiO$_2$ interface due to a strong charge transfer from the substrate to the N3 molecule. The assembling of positive charges at the surface of TiO$_2$ cause an upward bending of the energy bands.
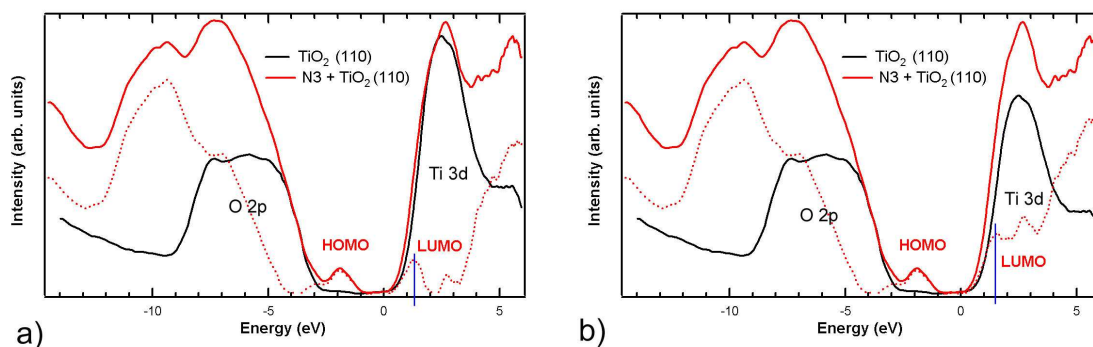

Figure 4.8: UPS and IPS of a clean and a dye/TiO$_2$(110) surface, where the clean surface spectra have been shifted and scaled. (a) Clean IPS spectra scaled by 0.98 (b) clean IPS spectra scaled by 0.78

To compare the clean and the dye sensitized surfaces, we shift the curves of the clean surface by 0.6 eV. The band edges of the valence band and conduction band are loacted after the shift at -2.8 eV and 0.8 eV, respectively. In the conduction band a broadening of the Ti-3d feature is visible, which can indicate the presents of a LUMO state. To accentuate specific changes in intensity due to the N3 adsorbate, we subtract the curve of the dye covered surface from the curve of the clean surface. The difference of intensity of these two spectra is shown in Fig. 4.8. Both curves are scaled to each other in a way that the curve for the clean surface does never exceeds the curve of the dye covered surface. In the case of the IPS spectra it is difficult to choose a definite scaling since contributions of the N3 dye span over the whole energy range of the inverse spectrum. In Figs. 4.8 (a) and (b) two possible scalings of the curve for the clean surface are shown. Once the subtraction is performed, the center of the LUMO is determined for (a) at 1.3 eV and (b) at 1.5 eV. As will be seen later, the existence of the N3 LUMO is confirmed by repeated measurements and by measurements of N3 on ZnO (see Fig. 4.16). A further characteristic difference in the spectrum is the broad peak in the higher energy regions (3-6 eV), which can be associated with unoccupied dye levels of higher energy.
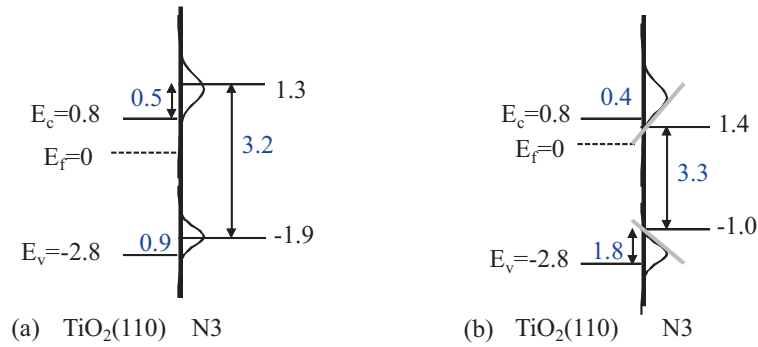

Figure 4.9: Electronic level alignment between the (a) center and (b) edges of the HOMO and LUMO and the rutile $TiO_2(110)$ VBM and CBM. The energies of the clean surface were shifted by 0.6 eV and energies in the diagram are given in eV.

With the information provided bu these UPS/IPS measurements, a more detailed characterization of the energy level alignment between the adsorbed N3 molecule on the TiO$_2$ surface can be achieved. The center of the HOMO state is 0.9 eV above the VBM and the LUMO center is 0.5 eV above the CBM. The energy difference between the HOMO center and the LUMO center is 3.2 eV.

The edges of the HOMO and the LUMO states are determined by linear fits, similar to what was done for the clean TiO$_2$ surface. Applying this procedure, we found the high energy edge of the HOMO 1.8 eV above the VBM and the low energy edge of the LUMO 0.4 eV below the TiO$_2$ CBM. The minimal band gap of the HOMO and the LUMO is determined to be 1.4 eV.

To produce current in a DSSC, an electron has to be excited from the HOMO to the LUMO and be transferred into the semiconductor. When we assume that the electron has to be at least at the same energy level as the CBM in order to be transferred into the semiconductor, the minimal required energy for current can be identified by the energy difference of the HOMO maximum and the CBM, which is determined to be 1.7 eV. By photon absorption an exciton is possibly created in the dye molecule, which reduces the minimal required excitation energy of an electron from the HOMO to the LUMO. This exciton however does not change the condition of an electron transfer that the energy level of the excited electron has to be at least at the same level as the CBM.

We note that caution must be used when attempting to compare numbers and optical absorption energies in real DSSC's. The presence of the electrolyte has an influence on the energetic structure of the orbitals of the dye molecule and increases the energetic HOMO-LUMO gap [56].

As described in section 4.12, to produce the dye covered surface measured here, the UHV cleaned TiO$_2$ surface undergoes several steps. To check if the obtained HOMO and LUMO states really originate from the dye, UPS and IPS spectra after each different intermediate step were taken. In Fig. 4.10 the unshifted spectra of clean TiO$_2$, TiO$_2$
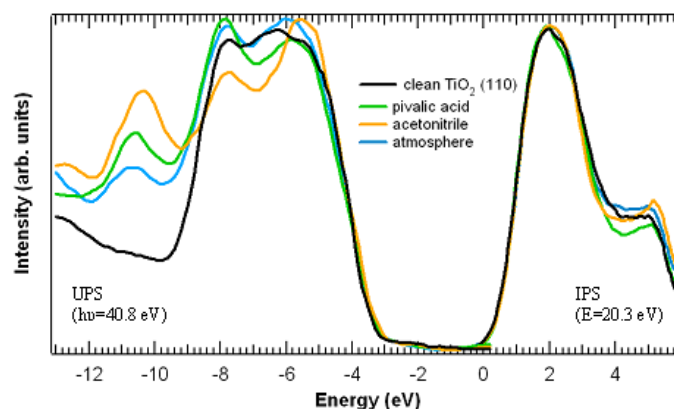
Figure 4.10: Comparison of UPS and IPS of clean $TiO_2(110)$ and $TiO_2(110)$ exposed to pivalic acid, acetonitrile, and atmosphere.

exposed to atmosphere, TiO_2 exposed to pivalic acid and TiO_2 exposed to acetonitrile are shown. All spectra, compared to the spectra from the clean surface, have contributions in the energy region -11 eV to -10 eV which are believed to originate from -OH groups of water [29]. In the energy range above 3.5 eV, the shape of the conduction band is slightly altered for the pivalic acid/TiO_2 and the acetonitrile/TiO_2 surface compared to the clean TiO_2 surface. The most important aspects however are the following: First, none of the UPS spectra have a contribution in the band gap. Secondly, the IPS spectra are not significantly different to the clean surface in the energy range of 0 to 3.5 eV. From these observations we can conclude that the features we attribute to the HOMO and LUMO, as well as the dipole shift are associated with N3 on the surface.

4.2.3 N3/anatase TiO_2 nanoparticles

With the same method that what used for N3/$TiO_2(110)$ single crystal, the electronic level alignment of N3/anatase TiO_2 nanoparticle can be determined. Fig. 4.11 shows UPS and IPS spectra of these clean and dye covered surfaces. The nanoparticles were not passivated before sensitizing with N3, since there are no significant qualitative differences
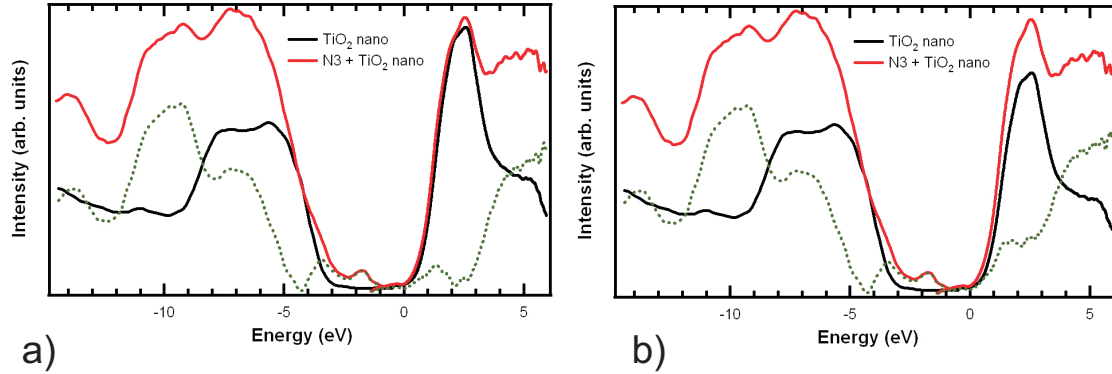
Figure 4.11: UPS and IPS of clean and dye/anatase TiO$_2$ nanoparticle surfaces, where the clean surface spectra have been shifted and scaled. The dashed line represents the difference of these two curves. (a) Clean IPS curve scaled by 0.97 (b) clean IPS curve scaled by a factor of 0.80

for the N3/TiO$_2$ system whether the TiO$_2$ substrate was passivated or not (the effect of passivation for TiO$_2$ is discussed in detail in section 3.7).

As in the previous analysis, the shift of the sensitized to the clean spectra is determined by the position of the Ti 3d feature and value of approximately 0.1 eV was found (0.1 eV is also the error/inaccurateness of the measurements). Compared to the shift in the N3/TiO$_2$(110) single crystal system (0.6 eV), the shift for the N3/TiO$_2$ nanoparticle system is significantly smaller. This can be explained by a weaker interface dipole caused by the small size of the nanoparticles (12-15 nm). The band bending in the TiO$_2$(110) takes place over a region that is in the order of 100 nm wide. Thus, in the nanoparticles there is not sufficient width for the charge carriers in the TiO$_2$ to rearrange and fully bend the band upward. [3] After the shift of the clean spectra, the position of the VBM is located at -3.2 eV and the position of the CBM is located at 0.6 eV. Thus,we determine a band gap of 3.8 eV for the nanoparticle film, which is about 0.2 eV larger than the band gap of rutile TiO$_2$(110). This change in measured gap is comparable what is found from optical measurements where the band gap of anatase (3.2 eV) is 0.2 eV larger than the band gap of rutile TiO$_2$ (3.0 eV) [25] [34].

Again, to accentuate specific changes in intensity due to the N3 adsorbate, we sub-tract the curve of the dye covered surface from the curve of the clean surface, which is shown in Fig. 4.11. Two different scalings of the IPS spectra were performed, since a definite scale factor of the clean IPS spectrum could not been determined. In both cases the position of the minimum and the center of the LUMO almost identical.
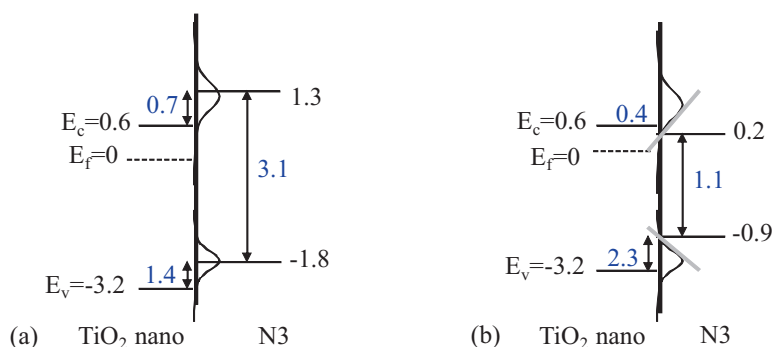

Figure 4.12: Electronic level alignment of the HOMO LUMO (a) centers and (b) edges of the N3/anatase TiO_2 nanoparticle system. Energies are given in eV.

Using UPS and IPS measurements a more detailed characterization of the electronic level alignments can be provided. A schematic diagram of the energy alignment is shown in Fig. 4.12. The center of the HOMO is found to be 1.4 eV above the VBM and the center of the LUMO is 0.7 eV above the CBM. The energy difference between the HOMO center and the LUMO center is determined to be 3.1 eV.

The high energy edge of the HOMO is located 2.3 eV above the CBM, the low energy edge of the LUMO is located 0.4 eV below the CBM, resulting in a the minimum HOMO-LUMO gap of 1.1 eV. The energy difference between the HOMO maximum and the conduction band minimum is about 1.5 eV.

4.2.4 INA/TiO$_2$(110) single crystal

The electronic level alignment of INA/rutile TiO_2(110) was also investigated. We studied the INA molecule because it is the analog to the linker of N3 and the spatial distribution of the N3 LUMO is thought to be arranged in the region of this ligand. Fig. 4.13 shows
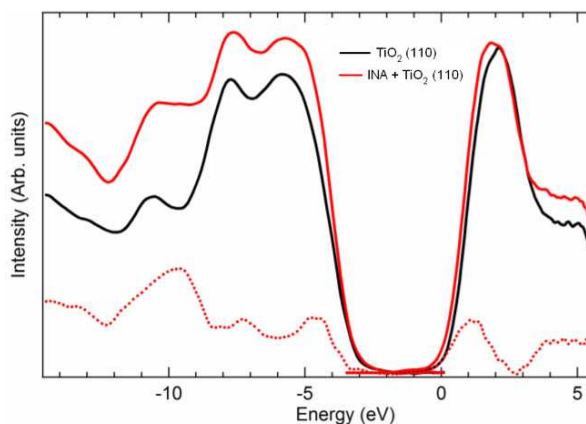
Figure 4.13: UPS and IPS spectra of a clean and a INA/rutile TiO$_2$(110) surface.

a UPS/IPS spectra of a clean and an INA covered TiO$_2$(110) surface. Both spectra were scaled to each other so that the curve of the INA covered surface nowhere exceeds the curve of the clean surface. In the curve for the clean surface, an additional contribution to the O 2p orbital in the region of -11 eV is visible. This is an indication that traces of water are still present on the surface and that probably the sample was not fully degased.

Our observations of the occupied and unoccupied states of INA absorbed on TiO$_2$ supports the notion of the metal-to-ligand charge transfer of the N3 molecule upon HOMO to LUMO excitation. The LUMO state of INA is found to be centered at the same energy region of 1.0 eV above the CBM and is of similar intensity as the LUMO of the N3 dye. This observance reinforces the idea that the spatial distribution of the LUMO is located around the pyridine/carboxyl complex of the N3 molecule. In contrast, the spatial distribution of the N3 HOMO is located separately around the Ru atom and along the thiocyanate chain (see section 3.2.1 and 3.3.1). The INA molecule does not possess these elements and so it is not surprising that the HOMO of the INA molecule is completely different to the HOMO of the N3 dye. No electronic contributions of the INA molecule are found in the energy region of the TiO$_2$(110) band gap.
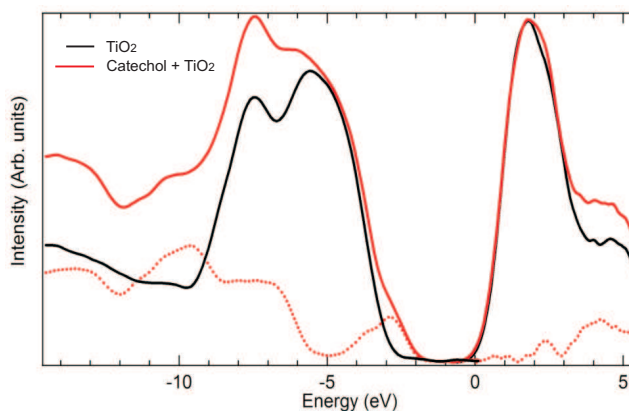
Figure 4.14: UPS and IPS spectra of clean and catechol/rutile $TiO_2(110)$ surfaces.

4.2.5 Catechol/TiO$_2$(110) single crystal

In Fig. 4.14 the spectra of a clean and a catechol covered $TiO_2(110)$ surfaces are presented. As indicated in section 4.12, the vapor pressure of catechol is high enough to expose the molecule directly in UHV to the titanium dioxide surface. The spectra of both surfaces were scaled that the curve of the clean surface nowhere exceeds the curve of the catechol covered surface. Since the position of the Ti $3d$ feature is identical for both spectra, no shift was performed. The HOMO of catechol is clearly visible near the valence band maximum and is centered at -3.1 eV. In the low energy range of the conduction band a smaller feature is observable centered at 2.3 eV. No strong statements about its existence can be made since it is only a small feature and the catechol/ZnO(11$\bar{2}$0) system seems to have a different behavior in the conduction band region. Above an energy of 3 eV, a more clearly contribution of catechol is recognizable centered at 4.1 eV. If we assume that the first LUMO feature is real 1.8 eV above the CBM, then the HOMO and the LUMO have a minimum energy difference of 3.3 eV.

Fig. 4.15 represents the electronic level alignment of the catechol/rutile $TiO_2(110)$ system. The center of the HOMO state is located 0.2 eV above the VBM and the center of the LUMO state is located 1.8 eV above the CBM. The energy difference of
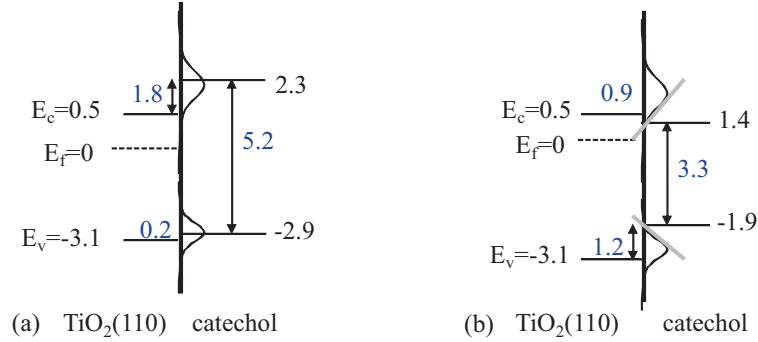
Figure 4.15: Electronic level alignment between the (a) center and (b) edges of the HOMO and LUMO and the TiO_2 VBM and CBM. Energies are given in eV.

the HOMO-LUMO centers is therefore 5.2 eV. The high energy edge of the HOMO is located 1.1 eV above the CBM and the low energy edge of the LUMO is located 0.9 eV above the CBM, which leads to a minimum HOMO-LUMO gap of 3.3 eV. If the strong electronic coupling between the catechol and the TiO_2 cause a direct charge transfer from the catechol to the semiconductor, then we have to examine the enregy difference between the HOMO and the CBM. Without taking excitons into account, the minimum required energy of a photon to produce current from our UPS/IPS measurements is the energy difference of the HOMO maximum and the CBM, which is found to be 2.4 eV. It is an open question whether excitons are created or not at a direct electron excitation from the HOMO to the CBM. Our obtained value of 2.4 eV (517 nm) however is very close to the optical absorption threshold of 500 nm from the literature (see Fig. 3.16 [51]).

4.3 Dye/ZnO results: Electronic Level Alignment

4.3.1 N3/ZnO(11$\bar{2}$0) single crystal

In Fig. 4.16 the spectra of a clean and a N3 dye covered ZnO(11$\bar{2}$0) single crystal surface are shown. The sample was passivated before sensitizing with N3. This treatment greatly improve the N3/ZnO(11$\bar{2}$0) interface (the effect of passivation on the electronic structure
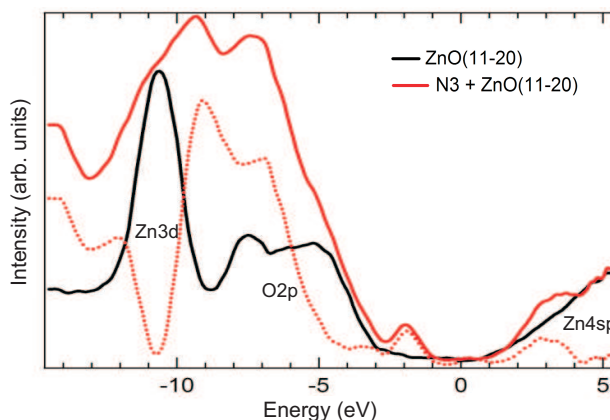
Figure 4.16: UPS and IPS of clean and dye/ZnO(11$\bar{2}$0) surface.

of ZnO is discussed in more detail in section 4.4.2). The valence band of the clean surface consists of a Zn $3d$ core level at an energy of -11 eV and orbitals of O $2p$ character in the range of -9 eV to -3 eV. The conduction band of the clean surface is a mixture of Zn $4s$ and Zn $4p$ orbitals, which are rather featureless. The absence of any sharp features and the low cross section of the Zn $4s$ and Zn $4p$ orbitals make zinc oxide a good candidate for a direct observation of the N3 LUMO state in IPS spectra.

Using the linear fit method as was done for TiO$_2$, we found the edge of the ZnO valence band at -3.0 eV and the edge of the ZnO conduction band at 0.6 eV, which results in a band gap of 3.6 eV. No band bending is observed for N3 on ZnO single crystal. The HOMO is clearly observable in the UPS spectrum and is centered at -1.9 eV. Since the Zn $3d$ feature in the N3/ZnO(11$\bar{2}$0) spectra is no longer visible, it could be that a coverage of one monolayer N3 is present on the ZnO surface and/or that the UPS measurement is too surface sensitive. The peak of the LUMO state of the N3 dye is clearly visible centerd at 3.1 eV and provides a confirmation for the existence of the LUMO state in the N3/TiO$_2$ system. The LUMO of the N3/ZnO(11$\bar{2}$0) system is much broader than LUMO of the N3/TiO$_2$ system, which can be explained by the different bonding of N3 to the semiconductors. The LUMO of N3 on TiO$_2$ is also believed to mix partly with the conduction band of TiO$_2$. The conduction band of ZnO is mixture of

Zn $4s$ and Zn $4p$ orbitals, whereat the conduction band of TiO_2 consist of states with Ti $3d$ orbital character.
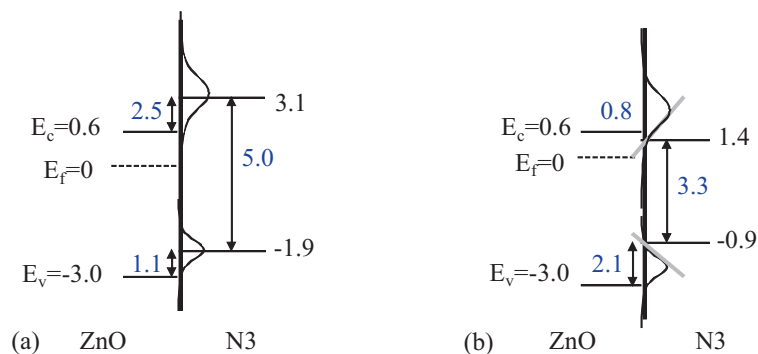

Figure 4.17: Electronic level alignment between the (a) center and (b) edges of the N3-HOMO and N3-LUMO and the $ZnO(11\bar{2}0)$ VBM and CBM. Energies are given in eV.

In Fig. 4.17 the electronic level alignment of the $N3/ZnO(11\bar{2}0)$ system is presented. The center of the HOMO state is located 1.1 eV above the VBM, the center of the LUMO state is located 2.5 eV above the CBM, which leads to a HOMO-LUMO energy difference of 5.0 eV.

The high energy edge of the HOMO is 2.1 eV above the VBM and the low energy of the LUMO is 0.8 eV above the CBM. The minimal energy difference of the HOMO and the LUMO is therefore 2.3 eV.

As for TiO_2, the clean ZnO sample undergoes several different steps before the surface is covered with N3 dye. To check if the HOMO and LUMO states really originate from the N3 molecule, UPS and IPS spectra were of a clean ZnO, an atmosphere/ZnO and a acetonitrile/ZnO surface were taken, which ar shown in Fig. 4.18. We fist not that none of the spectra have contributions in the region of ZnO band gap (-3 to 0 eV). The atmosphere/ZnO and acetonitrile/ZnO spectra have indeed some contributions in the region of the conduction band, but they are rather small and located more in a higher energy range than where the N3 LUMO is observed. For none of the curves was a shift
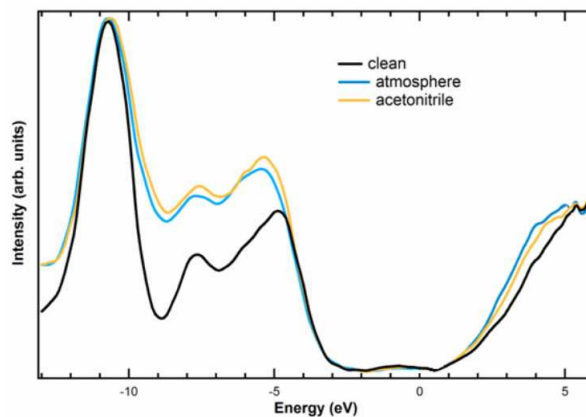
Figure 4.18: Spectra of the intermediate steps for a $ZnO(11\bar{2}0)$ single crystal surface.

observable. The existence of the HOMO and LUMO can therefore be assigned to the N3 molecules.

4.3.2 N3/ZnO nanorods
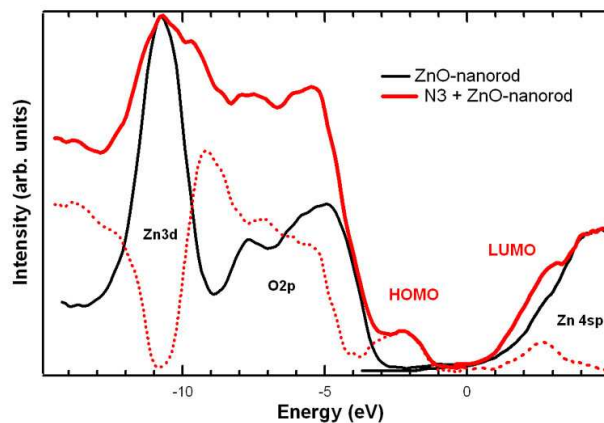
Figure 4.19: UPS and IPS spectra of a clean and a dye/ZnO nanorod surface.

In Fig. 4.19, UPS/IPS spectra of a clean and a N3 covered ZnO nanorod surface are presented. The spectra of the clean ZnO nanorod surface is nearly identical to the clean $ZnO(11\bar{2}0)$ surface. The valence band consists of a Zn $3d$ and a O $2p$ feature and the

conduction band consists of a mixture of Zn $4s$ and Zn $4p$ orbitals. The band gap of 3.7 eV is the same as for the ZnO($11\bar{2}0$) sample.

In these spectra, there is no evidence of a shift in the oxide features upon dye absorption. To emphasize the dye-induced features, a difference curve was directly calculated. The spectra were again scaled to each other in a way, that the curve of the clean surface exceeds nowhere the curve of the dye covered surface. The HOMO, as well as the LUMO are clearly visible and are very similar to the HOMO and LUMO of the N3/ ZnO($11\bar{2}0$) single crystal system.
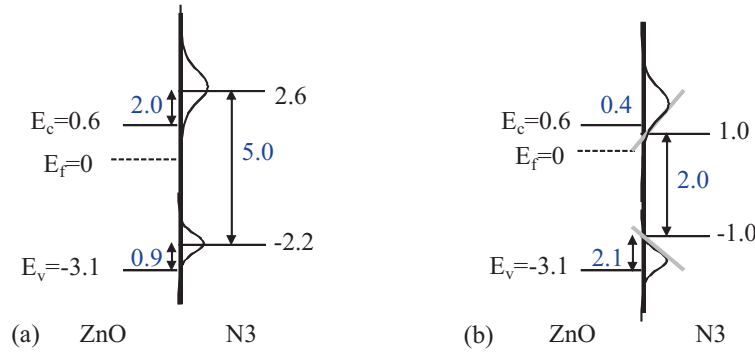

Figure 4.20: Electronic level alignment of the N3/ZnO nanorod (a) center and (b) edges of the HOMO and LUMO. Energies are given in eV.

From the UPS/IPS measurements a more detailed characterization of the electronic level alignment can be performed again. A schematic diagram of the energy levels is shown in Fig. 4.20. The center of the HOMO is 0.9 eV above the VBM, the center of the LUMO is 2.0 eV above the CBM. The energy difference between the HOMO center and the LUMO center was determined to be 4.8 eV.

The high energy edge of the HOMO is located 2.1 eV above the VBM, the low energy edge of the LUMO is located 0.4 eV and the minimal distance between the HOMO and the LUMO is determined to be 2.0 eV. Since the LUMO minimum is above the CBM, the minimal energy difference of the HOMO and the LUMO is also the minimal required energy to create current.

4.3.3   INA/ZnO(11$\bar{2}$0) single crystal
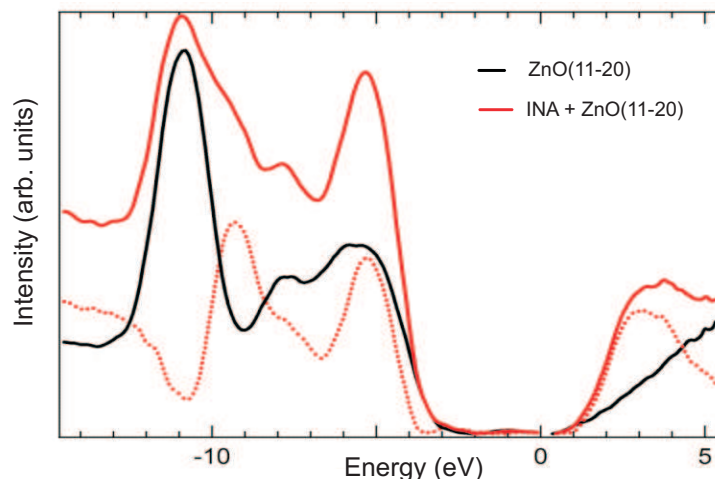
Figure 4.21: (a)UPS and IPS of clean and INA/ZnO(11$\bar{2}$0) single crystal surface.

We studied the isonicotinic acid molecule also in connection with ZnO(11$\bar{2}$0) single crystal, in order to, once again, compare the electronic structure with the N3 dye molecule. In Fig. 4.21, the spectra of a clean and an INA covered surface is shown. The spectra were scaled in a way that the curve of the clean surface never exceeds the curve of the INA covered surface. Since the positions of the Zn $3d$ orbitals were identical for both spectra, no band bending is observed. As for the INA/TiO$_2$ system, no contributions of the INA molecule in the energy range of the semiconductor band gap are present. The LUMO is clearly visible and centered at 3.1 eV. As compared to the N3/ZnO(11$\bar{2}$0) system, the LUMO of the INA contributes much more spectral intensity in the IPS spectra. Dispite this intensity difference, the identical position and the similar shapes of the LUMO of INA/ZnO(11$\bar{2}$0) reenforces the idea that spatial distribution is located around this pyridine/carboxyl complex. It is amazing that the binding ligand of the N3 dye can be separated from the rest of the molecule and still has almost the same electronic structure of the LUMO. The HOMO of the N3 dye has its spatially distribution around the Ru atom and along the thiocyante chain (see section 3.2.1 and

3.3.1). The INA molecule does not possess these elements and so it is not surprising that the HOMO of the INA molecule is completely different to the HOMO of the N3 dye. No electronic contributions of the INA molecule are found in the energy region of the ZnO(11$\bar{2}$0) band gap.
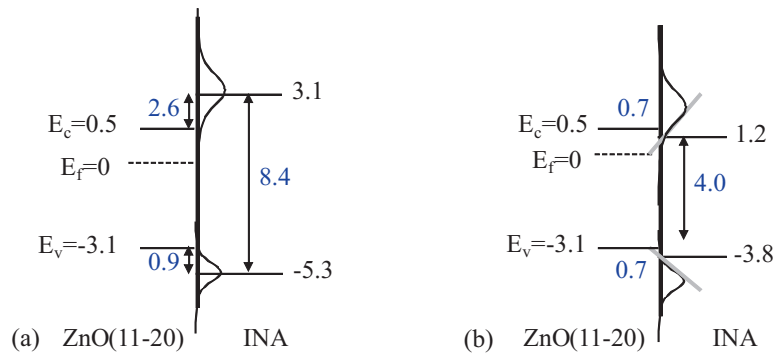

Figure 4.22: Electronic level alignment between the (a)center and (b)edges of the INA HOMO and LUMO and the ZnO VBM and CBM. Energies are given in eV.

In Fig. 4.22, the electronic level alignment of INA is shown for the region of the band gap.
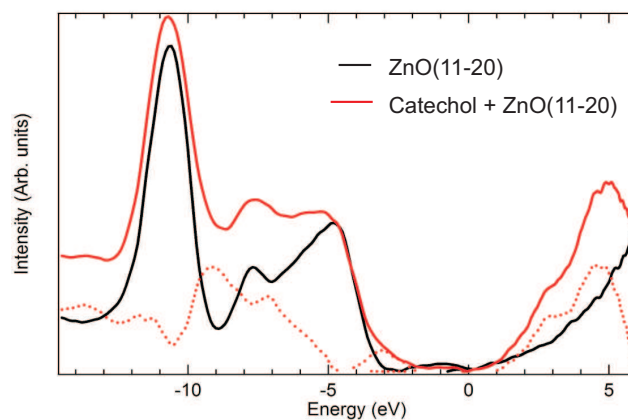
4.3.4 Catechol/ZnO(11$\bar{2}$0) single crystal

Figure 4.23: UPS and IPS spectra of a clean and a catechol/ZnO(11$\bar{2}$0) surface.

In Fig. 4.23 the spectra of a clean and a catechol covered $ZnO(11\bar{2}0)$ surface are shown. The scaling was performed in a way that the curve of the clean surface exceeds nowhere the curve of the catechol covered surface. Since the position of the Zn $3d$ orbitals is the same for both spectra, no shift was applied. After the subtraction, clear contributions of the catechol molecule are visible in the valence band, as well as in the conduction band. The HOMO is located close to the valence band inside the band gap and its center is determined to be at -3.1 eV. In the IPS spectra, there appear to be two LUMO features within a few eV of the Fermi level. The spectra of the catechol/$ZnO(11\bar{2}0)$ system differs in the LUMO, but agrees with the HOMO contributions of the catechol/$TiO_2(110)$ system. This makes actually sense, since the two semiconductor have the same type of valence band (O $2p$ features) and differ in their type of conduction band. In addition, it has been reported that catechol bonds strongly to TiO_2 and that its LUMO is mixed with the TiO_2 conduction band [51].
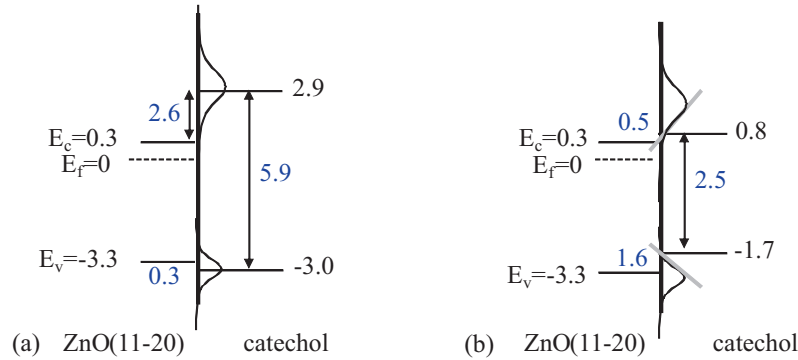
Figure 4.24: UPS and IPS spectra of clean and catechol/$ZnO(11\bar{2}0)$ surface. Energies are given in eV.

From the UPS and IPS measurements a more detailed characterization of the electronic level alignment can be performed. A schematic diagram of the energy levels is shown in Fig. 4.24. The center of the HOMO is located 0.3 eV above the VBM and the center of the first LUMO is located 2.6 eV above the CBM. The energy difference of the HOMO-LUMO center is about 5.9 eV. The high energy edge of the HOMO is 1.6 eV above the VBM, the low energy edge of the LUMO is 0.5 eV above the CBM, which

leads to a minimal HOMO-LUMO energy difference of about 2.5 eV.

4.4 Effect of passivation on electronic structure

4.4.1 TiO$_2$(110) single crystal
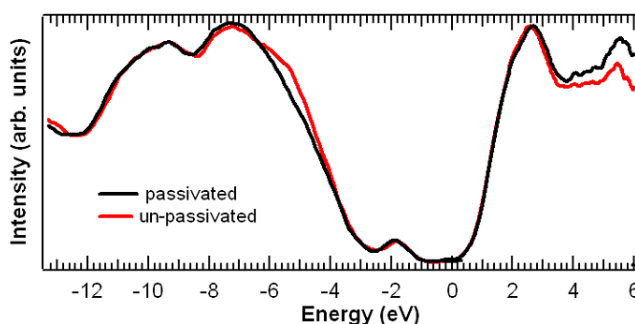
Figure 4.25: UPS and IPS spectra of a passivated and a non-passivated N3/rutile TiO$_2$(110) surface.

To estimate the effect of surface passivation on the electronic structure, the rutile TiO$_2$(110) single crystal sample was sensitized with and without previous passivation. Fig. 4.25 shows that UPS and IPS spectra of these two surfaces are very similar in the region of the HOMO and LUMO states. Some differences are observable in the region of -6 to - 4 eV, as well as in the region of 3 to 6 eV. These differences can have several possible origins: the dye concentration on the TiO$_2$(110) surface could differ easily and the non-passivated surface could still contain impurities from the atmosphere. It seems however, that in the end the passivation of the TiO$_2$ surface does not have much effect on the quality of the N3/TiO$_2$ interface.
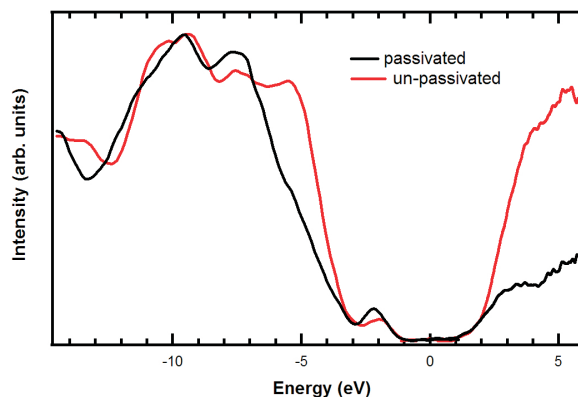
Figure 4.26: UPS and IPS spectra of a passivated and non-passivated N3/ZnO(11$\bar{2}$0) single crystal surface

4.4.2 ZnO(11$\bar{2}$0) single crystal

To estimate the effect of passivation on a ZnO(11$\bar{2}$0) single crystal surface, the ZnO sample was sensitized with and without prior passivation. Fig. 4.26 presents these two spectra, which clearly differ from each other. The non-passivated surface possess higher intensity as the passivated surface in the region -7 to -3 eV, as well as in the region above 2 eV. We attribute these contributions to atmospheric contaminants. A difference in dye concentration can hereby not be excluded. The passivation of the ZnO(11$\bar{2}$0) single crystal surface is thus very important for the quality of the N3/ZnO interface.

4.4.3 Conclusions

In this chapter, a detailed method of measuring the energy level alignment between molecular adsorbates and oxide substrates has been discussed. By measuring the occupied and unoccupied electronic states directly, we determined the energy level alignment of several adsorbate/oxide systems relevant to DSSC's. Results were presented of three different molecules (N3, INA, catechol) absorbed on rutile TiO$_2$(110) single crystal and ZnO(11$\bar{2}$0) single crystal, as well as N3 absorbed on anatase TiO$_2$ nanoparicles and ZnO nanopillars. The electronic structure of clean rutile TiO$_2$ single crystal was very similar

to the electronic structure of anatase TiO_2 nanoparticles. The electronic contributions of the N3 dye absorbed on the surface were also very similar for both different substrates. The many different ways of N3 molecules bonding to the TiO_2 surface may be an explanation for this result and also an explanation for the broadness of the N3 electronic features. The UPS/IPS spectra of ZnO single crystal and ZnO nanopillars bear also strong resemblances to each other. The unoccupied DOS of N3 on ZnO has been shown to differ from that of N3 on TiO_2. The LUMO of N3 on TiO_2 has been shown to be much closer to the CBM, resulting to a smaller HOMO-LUMO gap compared to N3 on ZnO. This can be attributed to the different character of the TiO_2 and ZnO conduction bands, which would be expected to interact differently with the unoccupied states of N3. We have also measured the electronic structure of a INA, which is representative of a binding ligand of N3, on TiO_2 and ZnO. The comparisons between the occupied and unoccupied electronic structure of INA on TiO2(110) and $ZnO(11\bar{2}0)$ with those of N3 on the same substrates show that these two molecules have very different occupied electronic structure and similar unoccupied electronic structure. This result is in agreement with our expectations since the spatial distribution of the N3 LUMO is thought to be localized at this part of the molecule. It is reported that the catechol molecule binds very strong to the TiO_2 surface and mixes significantly its unoccupied density of states with the conduction band of TiO_2. Here again, since the conduction band of ZnO differs from the conduction band of TiO_2, it is expected and verified that the LUMO of the catechol/ZnO system shows big differences to the catechol/TiO_2 system.

Chapter 5

Discussion and Summary

5.1 Summary of the results

In table 5.1 and 5.2, the electronic alignment of the energy levels is summarized.

The literature value of the rutile TiO_2 single crystal optical band gap is 3.2 eV [25]. Our UPS/IPS spectra are directly related to the DOS of the semiconductor and the transport band gap of TiO_2 is here determined. The measured value of the $TiO_2(110)$ band gap is determined to be 3.6 eV, which has been confirmed by repeated measurements within the margin of errors. The discrepancy to the optical band gap could be explained by the absence of excitons in our measurements and by the different technique of data analysis. The transport band gap of anatase TiO_2 nanoparticle is 0.2 eV larger than the band gap of $TiO_2(110)$ single crystal. This difference in the measured band gap is comparable with what is known from optical measurements where the band gap of anatase TiO_2 nanoparticle (3.2 eV) is 0.2 eV larger than the band gap of rutile TiO_2 (3.0 eV) [34].

The literature value of the $ZnO(11\bar{2}0)$ optical band gap is 3.3 eV [38] [39] [40]. Our measured value of 3.6 eV is 0.3 eV larger than the literature value, which could be explained again by the absence of excitons and by different technique of data analysis. The band gap of the ZnO nanopillar is slightly larger than for the ZnO single crystals (3.7 eV).

	TiO$_2$(110)+N3	TiO$_2$-np+N3	TiO$_2$(110)+Catechol	TiO$_2$(110)+INA
VBM	-2.8	-3.2	-3.1	-3.2
CBM	0.8	0.6	0.5	0.4
bandgap	3.6	3.8	3.6	3.6
HOMO center	-1.9	-1.8	-3.1	-4.6
HOMO max	-1.0	-0.9	-1.9	-3.4
LUMO min	0.4	0.2	1.4	-0.2
LUMO center	1.3	1.3	2.3	
HOMO-LUMO	3.2	3.1	5.4	
min HOMO-LUMO	1.4	1.1	3.3	2.3
shift	0.6	0.1	0	0

Table 5.1: Electronic level alignment of dye/TiO$_2$. The values are given in units of eV, the abbreviation np stands for nanoparticle. The error of the measured values is about $\pm$ 0.1 eV, the error of the energy differences is about $\pm$ 0.2 eV.

	ZnO(11$\bar{2}$0)+N3	ZnO-nr+N3	ZnO(11$\bar{2}$0)+Catechol	ZnO(11$\bar{2}$0)+INA
VBM	-3.0	-3.1	-3.3	-3.1
CBM	0.6	0.6	0.3	0.5
bandgap	3.6	3.7	3.6	3.6
HOMO center	-1.9	-2.2	-3.0	- 5.3
HOMO max	-0.9	-1.0	-1.7	-3.8
LUMO min	1.4	1.0	0.8	1.2
LUMO center	3.1	2.6	2.9	3.1
HOMO-LUMO	5.0	4.8	5.9	8.4
min HOMO-LUMO	2.3	2.0	2.5	5.0
shift	0	0	0	0

Table 5.2: Electronic level alignment of dye/ZnO. The values are given in units of eV, the abbreviation nr stands for nanorod. The error of the measured values is about $\pm$ 0.1 eV, the error of the energy differences is about $\pm$ 0.2 eV.

The smallest value of 1.1 eV for the minimum HOMO-LUMO gap is found for the TiO$_2$ nanoparticle sample in connection with N3 dye. The N3 molecule has in combination with TiO$_2$(110) single crystal a similar value for the minimum HOMO-LUMO gap of 1.4 eV. The minimal HOMO-LUMO energy difference is for both ZnO structures identical and with a value of 2.0 eV significantly larger than what was found for TiO$_2$. The catechol/TiO$_2$(110) system has, in this aspect, a quite large value of 3.3 eV, but due to the strong electronic coupling it is suggested that a direct electron transfer into the semiconductor is possible [52]. The more important value is the energy difference between the HOMO maximum and the CBM, which had been determined to be 2.4 eV.

5.2 Comparison with literature
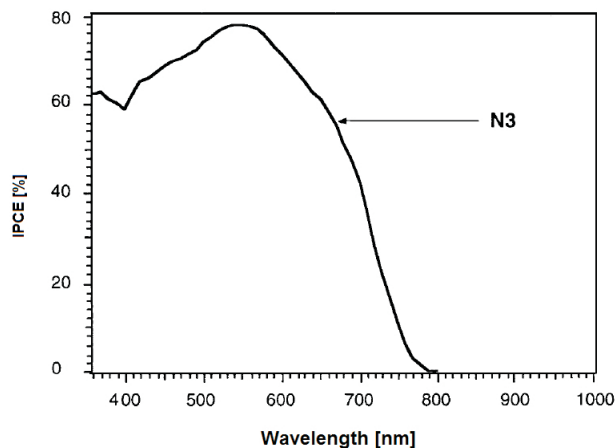
Figure 5.1: IPCE vs. photon energy for a DSSC with N3 [4].

One of the complementary measurements to our UPS/IPS experiments is the study of the incident photon to current efficiency (IPCE) of a solar cell. With this measurement technique, light of a certain wavelength is directed onto the DSSC. The wavelength of the incident light is increased stepwise and the efficiency of the DSSC is measured. Before we can compare our results with this experiment, we have to bear several things in mind. In absorption measurements, the presence of excitons has always to be taken into account.

Our UPS/IPS techniques avoid these excitons and the taken spectra are closely related to the DOS of the system in ground state. Furthermore, the presence of an electrolyte solution in a DSSC has influence on the electronic structure of the N3 dye and increases its energetic HOMO-LUMO gap [56].

Fig. 5.1 shows an ICPE spectra of a N3 covered on an anatase TiO_2 nanoparticle surface [4]. For us the edge of the spectra is interesting, since there the photons are able for the first time to produce electricity and this value can be compared with our results. The limit wavelength for N3 in this measurement is 780 nm, which corresponds to energy of 1.6 eV. From our energy level arrangement, the minimal required energy to produce current is 1.5 eV. This value is only an approximation and corresponds to the energy difference between the HOMO maximum and the CBM. An electron is excited from the HOMO to the LUMO and transferred into the semiconductor. To generate electricity, the electron has to diffuse through the semiconductor and reach the electrode. Although the conditions of our experiment differ from ICPE measurements from Grätzel, the obtained values agree quite well.

Summary

We used the combination of IPS and UPS to measure the energy level alignment for organic dye/oxide systems. We measured the energy level alignment for N3/TiO_2(110), N3/TiO_2 nanoparticle, INA/TiO_2(110), catechol/TiO_2(110), N3/ZnO(11$\bar{2}$0), N3/ZnO nanopillar, INA/ZnO(11$\bar{2}$0) and catechol/ZnO(11$\bar{2}$0) systems. The semiconductor surfaces for N3 and INA exposure were prepared by passivating clean, well-ordered oxide substrates with pivalic acid to reduce atmospheric and solution contamination during the deposition of the molecular overlayers. This passivation was shown to preserve the morphology of the oxide layers during these exposures by STM imaging. Catechol has a high enough vapor pressure to be exposed directly in UHV to the semiconductor. In order to find the energy level alignment between the adsorbed molecules and the oxide

substrate, we measured the UPS and IPS spectra from both the clean and molecule covered oxide surfaces. For all N3/oxide systems, the HOMO of the N3 molecule is clearly visible and locaced deep inside the energy region of the oxide band gap. The LUMO of N3 on TiO_2 could only be clearly observed by subtracting the IPS spectrum from the clean surface from that of the N3 covered surface and is located very close to the CBM of TiO_2. The energy level alignment between N3 dye and TiO_2 nanoparticles was very similar to that between N3 and $TiO_2(110)$, particularly for the LUMO and the CBM. The small HOMO-LUMO band gap of 1.4 eV and 1.1 eV for N3/$TiO_2(110)$ and N3/TiO_2 nanoparticle film, respectively, allows a DSSC to absorb a large part of the visible solar spectrum. An interesting difference between the N3/$TiO_2(110)$ and N3/TiO_2 nanoparticle systems was that the TiO_2 bands were found to bend upward in the N3/$TiO_2(110)$ system by 0.6 eV, while those in the N3/TiO_2 nanoparticle system were found to bend upward only by 0.1 eV. The upward band bending in the N3/$TiO_2(110)$ was explained by a positive screening charge in the surface region (100 nm) of the TiO_2 that was induced by electron transfer to the N3 molecules due to chemical bonding. The smaller band bending in the TiO_2 nanoparticle substrate was attributed to the small size (15 nm) of the nanoparticles, which are not large enough to allow for the full upward band bending to take place. In the IPs spectrum of N3/ZnO the LUMO was already clear visible without previous subtraction of the curves, which can be explained by featurelessness and low cross section of the ZnO conduction band states. The HOMO is very similar in both oxide cases, but differences can be observed in the LUMO. The LUMO for the N3/ZnO system is located further away from the CBM and has a broader shape than the LUMO of the N3/TiO_2 system. A possible explanation for these observations is that the N3 HOMO is localized at the center of the N3 molecule and has little interaction with the substrate, while the LUMO is localized on the part of the molecule that bonds to the substrate. Thus, the LUMO could be different in the N3/TiO2 and N3/ZnO systems due to the different orbital character of the TiO2 conduction band, which is largely composed of Ti 3d states, and the ZnO conduction band, which is largely composed of

Zn 4s and 4p states. It is interesting to study the INA molecule since it is the analog of the N3 binding ligand. When we take UPS and IPS spectra of the clean and the INA exposed TiO_2 and ZnO surface, we can find out that the INA does not give any contributions in the region of the band gap of the oxides and that its LUMO is very similar in position and intensity to the LUMO of the N3 molecule. This result enforces the theoretical model calculations, which claims that the LUMO of the N3 molecule is located separately to the HOMO at the pyridine/carboxylic acid complex. It is reported that the catechol molecule bonds strongly to the TiO_2 surface and that its unoccupied states mixture significantly with the conduction band of TiO_2 and that a direct charge transfer from the catechol HOMO to the conduction band of TiO_2 is possible. Since the conduction band of ZnO differs from the conduction band of TiO_2, we expect that catechol bonds in a different way, as already verified in the case of INA, to the ZnO surface. Indeed, the electronic structure of the unoccupied states differs significantly in both cases, but agrees in the occupied states.

References

[1] M. Grätzel; Solar cells to dye for;Nature Vol. 421, p. 586, 2003.

[2] M. Graetzel; Photoelectrochemical cells; Nature Vol. 414, Nov 2001.

[3] M.A. Green, K. Emery, D.L. King, S. Igari, and W. Warta; Solar Efficiency tables (vers. 23); Progress in Photovoltaics, Res. and Appl. 12:365, 2004.

[4] M. Grätzel. Progress in Photovoltaics: Res. and Appl.; 8:171, 2000.

[5] J.B. Asbury, E. Hao, Y. Wang, H.N. Ghosh, and T. Lian; J. Phys. Chem. B; 105:4545, 2001.

[6] S.Y. Huang, G. Schlichthorl, A.J. Nozik, M. Grätzel, and A.J. Frank.; J. Phys. Chem. B, 101:2576; 1997.

[7] Anderson NA, Lian TQ.; Ultrafast electron transfer at the molecule semiconductor nanoparticle interface; Annu. Rev. Phys. Chem. B 56:491-519; 2005.

[8] T. Hannappel, B. Burfeindt, W. Storck, F. Willig; Measurement of ultrafast photoinduced electron transfer from chemically anchored Ru-dye molecules into empty electronic states in a colloidal anatase TiO_2 film; Phys. Chem. B 101:6799-802; 1997.

[9] J.B. Asbury, E. Hao, Y. Wang, H.N. Ghosh and T. Lian; Ultrafast electron transfer dynamics from molecular adsorbates to semiconductornnocrystlline thin films; J. Phys. Chem. B. 2001, 105, 545-4557.

[10] T. Hannappel, B. Burfeindt, Winfried Storck, and F. Willig; Measurement of ultrafast photoinduced electron transfer from chemically anchored Ru-dye molecules into empty electronic states in a colloidal anatase TiO_2 film; J. Phys. Chem. B 1997, 101, 6799-6802.

[11] S.Y. Huang, G. Schlichthorl, A.J. Nozik, M. Grätzel, and A.J. Frank; Charge recombination in dye-sensitized nanocrystalline TiO2 solar cells; J. of Phys. Chem. B, 101:2576; 1997.

[12] B.A. Gregg, F. Pichot, S. Ferrere, and C.L. Fields; Interfacial Recombination Processes in Dye-Sensitized Solar Cells and Methods To Passivate the Interfaces; J. of Phys. Chem. B, 105:1422, 2001.

[13] J.M. Kroon, N.J. Bakker, H.J.P. Smit, P. Lisk, K.R. Thampi, P. Wang, S.M. Zakeeruddin, M. Grätzel, A. Hinsch, S. Hore, U. Würfel, R. Sastrawan, J.R. Durrant, E. Palomares, H. Pettersson, T. Gruszecki, J. Walther, K. Skupien and G.E. Tulloch; Nanocrystalline Dye-sensitized solar cells having maximum perfamnce; Prog. Photovolt: Res. Appl. 2007; 15:1-18.

[14] W.R. Duncan and O.V. Prezhdo; Theoretical studies of photoinduced electron transfer in dye-sensitized TiO_2; Phys. Chem. B 58:143-84; 2007.

[15] R. Katoh, A. Furube, A. V. Barzykin, H. Arakawa and M. Tachiya, Kinetics and mechanism of electron injection and charge recombination in dye-sensitized nanocrystalline semiconductors; Coordination Chemistry Reviews 248 (2004) 1195-1213.

[16] D.P. Woodruff and T.A. Delchar; Modern techniques of surface science; Cambridge 1989.

[17] J.C. Fuggle and J.E. Inglesfield; Unoccupied electronic states; Springer; Heidelberg 1992.

[18] P.D. Johnson and S.L. Hulbert; Normal incidence grating spectrometer designed for inverse photoemmssion studies in the range 10-30 eV; New York 1986

[19] H.G. Van Zyl; Modelling of integrated optic components for lightwave communications systems using the beam propagation method; Johannesburg 2001;

[20] C. J. Chen; Introduction to scanning tunneling microscopy; New York 1993.

[21] H. Haken, H.C. Wolf; Molekülphysik und Quantenchemie; Springer Berlin Heidelberg New York, 5th edition; 2006.

[22] A. Roth; Vacuum technology; 2nd edition; North Holland 1986.

[23] P.W. Palmberg; J. Vac. Sci. Tech., 12:379; 1974.

[24] G. Ertl and J. Kuppers; Low Energy Electrons and Surface Chemistry; Weinheim, 1985.

[25] K. M. Reddy, S.V. Manorama, A.R. Reddy: Bandgap studies on anatase titanium dioxide nanoparticles; Material Chemistry and Physics 78 (2002) 239-245.

[26] U. Diebold; The surface science of titanium dioxide; Surfce Science Reports 48 (2003) 53-229.

[27] A. Hagfeldt und M. Grätzel; Molecular Photovoltaics; Acc. Chem. Res 33, 269-277; 2000.

[28] U. Diebold and J.F. Anderson, K.O. Ng and D. Vanderbilt; Evidence for the tuneling site on transition-metal oxides: $TiO_2(110)$; 1996.

[29] T.J. Beck, A. Klust, M. Batzill, U. Diebold, C. Di Valentin, A. Tilocca and A. Selloni; Mixed dissociated/molecular monolayer of water on the $TiO_2(011)$-(2x1) surface; Surf. Sci. Letters, 591:L267; 2005.

[30] M. Li, W. Hebenstreit, L. Gross, U. Diebold, M.A. Henderson, D.R. Jennison, P.A. Schultz, M.P. Sears; Oxygen-induced restructing of the $TiO_2(110)$ surface: a comprehensive study; Surf. Science, 173-190; 1999.

[31] M. Ramamoorthy, D. Vanderbilt; First-priciples calculations of the energetics of stoichiometric TiO_2 surfaces; Phys. Rev. B49 (1994) 16721.

[32] M. Lazzeri, A. Vittadini and A. Selloni; Structure and energetics of stoichiometric TiO_2 anatase surfaces; Phys. Rev. B, Vol. 63, 155409, 2001.

[33] H. Zhang and J. F. Banfield; Thermodynamic analysis of phase stability in nanocrystalline titania; J. Mater. Chem. 8, 2073 (1998).

[34] L. Miao, P. Jin, K. Kaneko, A. Terai, N. Nabatova-Gabain, S. Tenemura; Preparation and characterization of polycrystalline anatase and rutile TiO_2 thin films by rf magnetron sputtering; Appl. Surf. Science 212-213(2003) 255-263.

[35] E. Galoppini, J. Rochford, H. Chen, G. Saraf, Y. Lu, A. Hagfeldt, and G. Boschloo; J. Phys. Chem. B Letters, 110:16159; 2006.

[36] B. Meyer and D. Marx; Density-functional structure ans stbility of ZnO surafces; Physical Review B 67, 035403; 2003.

[37] O. Dulub, L.A. Boatner, U. Diebold; STM study of the geometric and electronic structure of ZnO(0001)-Zn, (000$\bar{1}$)-O, (10$\bar{1}$, and (11$\bar{2}$0) surfaces; Surface Science 519 (2002) 201-217.

[38] C.L. Dong, C. Persson, L.Vayssieres, A. Augustsson, T.Shmitt, M. Mattesini, R. Ahuja, C.L. Chang and J.-H Guo; Electronic structure of nanostructured ZnO from X-ray absorption and emission spectroscopy and the local density approximation; Physical Review B 70, 195325; 2004.

[39] D.C. Look; Recent advances in ZnO materials and devices; Material Science and Engineering B80 (2001) 383-387.

[40] J.F. Muth, R.M. Kolbas, A.K. Sharma, S.Oktyabrsky and J. Narayan; Excitonic structure and absorption coefficient measurements of ZnO single crystal film deposited by pulsed laser deposition; Applied Physics, Vol. 85 Numb.11; 1999.

[41] S. Muthukumar, H. Sheng, J. Zhong, Z. Zhang, N.W. Emanetoglu and Y. Lu; Selective MOCVD Growth of ZnO nanotips; IEE Transactions on nanotechnology, Vol 2, No. 1; 2003.

[42] E. Gallopini, J. Rochford, H. Chen, G. Saraf, Y. Lu, A. Hagfeldt and G. Boschloo; Fast electron transport in metal organic vapor deposition grown dye-sensitized ZnO nanorod solar cells; Phys. Chem. B, 110, 16159-16161; 2006.

[43] O. Taratula, E. Galoppini, D. Wang, D. Chu, Z. Zhang, H. Chen, G. Saraf and Y. Lu; Binding studies of molecular linkers to ZnO and MgZnO Nanotip films; J. Phys. Chem. B 2006, 110, 6506-6515.

[44] A.B.F. Martinson, J.E. McGaraah, M.O.K. Parpia and J.T. Hupp; Dynamics of charge transport and recombination in ZnO nanorod array dye-sensitized solar cells; Phys. Chem. Chem. Phys., 2006, 8, 4655-4659.

[45] K. Keis, C. Bauer, G. Boschloo, A. Hagfeldt, K. Westmark, H. Resnmo, H. Siegbahn; Nanostructured ZnO electrodes for dye-sensitized solar cell applications; Journal of Photochemistry and Photobiology A: Chem. 148 (2002) 57-64.

[46] W. Stier, WR. Duncan, OV. Prezhdo; Ab initio molecular dynamics of ultrafast electron injection from molecular donors to the TiO_2 acceptor; SPIE Proc. 5223:132-46; 2003.

[47] A. Sasahara, C.L. Pang, H. Onishi; Stm observation of a ruthenium adsorbed on a $TiO_2(110)$ surface; J. Phys. Chem. B 100, 4751-4755; 2006.

[48] P. Persson and M.J. Lundqvist; Calculated structual and electronic interactions of the ruthenium dye N3 with a titanium dioxide nanocrystal; J. Phys Chem. B 109, 11918-11924; 2005.

[49] J.H. Snook, L.A. Samuelson, J. Kumar, Y.G. Kim, J.E.Whitten; Ultraviolet photoelectron spectroscopy of nanocrystalline TiO_2 films sensitized with (2,2'-bipyridyl)ruthenium(II) dyes for photovoltaic applications; Science Direct, Organic Electronics 6 (2005)55-64;

[50] A. Vittadini, A. Selloni, F. P. Rotzinger, and M. Grätzel; Formic Acid adsorption on dry and hydrated TiO_2 anatase (101) surfaces by DFT calculations; J. Phys. Chem. B 2000, 104, 1300-1306.

[51] P.Persson, R. Bergström, and S. Lunell; Quantum chemical study of photoinjection in dye-sensitized TiO_2 nanoparticles; J. Phys. Chem. B, 101, 10348-10351; 2000.

[52] W.R. Duncan and O.V. Prezhdo; Electronic structure and spectra of catechol and alizarin in the gas phase and attached to titanium; J. Phys. Chem., 109, 365-373; 2005.

[53] Y. Xu, W.K. Chen, S.H. Liu, M.J. Cao and J.Q. Li; Interaction of photoactive catechol with TiO_2 anatase (101) surface: A periopdic density functional theory study; ScienceDirect, Chem. Phys. 331, 275-282; 2007.

[54] G. Ramakrishna, S. Verma, D.A. Jose, D.K. Kumar, A. Das, D.K. Palit, and H.N. Ghosh; Interfacial electron transfer between the photoexcited porphyrin molecule and TiO$_2$ nanoparticles: Effect of catecholate binding; J. Phys. Chem. B. 2006, 110, 9012-9021.

[55] M. Batzill, E.H. Morales and U. Diebold; Influence of Nitrogen Doping on the defect formation and surface properties of TiO$_2$ rutile and anatase; Physical Review Letters 96, 026103; 2006.

[56] S. Fantacci, F. de Angelis, and A. Selloni; Absorption spectrum and solvachromism of [Ru(4.4'-COOH-2.2'-bpy)$_2$(NCS)$_2$] molecular dye by time dependent density functional theory;J. Am. Soc., 2002.

[57] M. K. Nazeeruddin, F. de Angelis, S. Fantacci, A. Selloni, G. Viscardi, P. Liska, S. Ito, B. Takeru, and M. Gräztel; Combined experimental and DFT-TDDFT computational study of photoelectrochemical cell ruthenium sensitizers; Am. Chem. Soc. 2005, 127, 16835-16847.

Chapter 6

APPENDIX:

6.1 Abbreviations

AES: Auger electron spectroscopy

CBM: Conduction band minimum

CEM: Channeltron electron multiplier

CMA: Cylindrical mirror analyzer

DSSC: Dye sensitized solar cell

FTO: Fluorinated tin oxide

HOMO: Highest occupied molecular orbital

INA: Isonicotinic acid

INDO: Intermediate neglect of differential overlap

IPCE: Incident-photon-to-current conversion efficiency

IPS: Inverse photoelectron spectroscopy

LUMO: Lowest unoccupied molecular orbital

MOCVD: metalorganic chemical vapor deposition

STM: Scanning tunneling microscopy

TCO: Transparent conducting oxide

UPS: Ultraviolet photoemission spectroscopy

V_{OC}: Open circuit voltage

VBM: Valence band maximum

6.2   Curriculum Vitae

Jean-Patrick Theisen

1994 to 2003	:	Werner-von-Siemens Gymnasium Weißenburg, Abitur (A levels)
Since Oct. 2004:		Study of physics at the University of Würzburg, Vordiplom (comparable to bachelor degree)
2007 to 2008	:	Graduate student at the University of Rutgers